

Mature dendritic cell-derived dendrosomes swallow oxaliplatin-loaded nanoparticles to boost immunogenic chemotherapy and tumor antigen-specific immunotherapy

Xing Chen^a, Xiang Ling^b, Jiaxuan Xia^a, Ying Zhu^a, Longlong Zhang^a, Yuwei He^a, Anni Wang^a, Guolong Gu^a, Bo Yin^{c,**}, Jianxin Wang^{a,d,*}

^a Department of Pharmaceutics, School of Pharmacy, Fudan University, Key Laboratory of Smart Drug Delivery, Ministry of Education, Shanghai, 201203, China

^b Department of Pharmaceutics, School of Pharmacy, China Pharmaceutical University, State Key Laboratory of Natural Medicines, Nanjing, 210009, China

^c Department of Radiology, Huashan Hospital, Fudan University, Shanghai, 200040, China

^d Institutes of Integrative Medicine of Fudan University, Shanghai, 200040, China

ARTICLE INFO

Keywords:

Dendritic cell
Dendrosome
Antigen delivery
Immunotherapy
Chemotherapy

ABSTRACT

The cytomembrane-derived delivery platform represents a promising biomimetic strategy in oncology. To achieve durable and reliable tumor inhibition, mature dendrosomes (mDs), which were isolated from bone marrow-derived dendritic cells undergoing CT26 tumor antigen (TA) stimulation, were fused with redox-responsive nanoparticles (NPs) that were composed of poly(disulfide ester amide) polymers with an intensified disulfide density and hydrophobic oxaliplatin (OXA) prodrugs with the ability to potentiate immunogenicity. *In vitro* and *in vivo* results revealed that NP/mDs could induce tumor cell death through mitochondrial pathway and thus created immunogenic microenvironments, but also elicited immunocyte differentiation by TA cross-dressing and infiltration by direct presentation. By further neutralizing immune-regulatory interaction, the administration of PD-L1 antibody (α PD-L1) greatly improved antitumor efficiency of NP/mDs. Furthermore, the effectors of host immune systems effectively inhibited the growth and metastasis of distal tumors, likely because the autologous TA evoked by OXA and allogeneic TA delivered by mDs acted as additional stimuli to reinforce the immune response of tumor-specific T cells and immunosurveillance toward oncogenesis. These results demonstrated that NP/mDs could simultaneously realize immunogenic chemotherapeutics and specific TA delivery. In combination with α PD-L1, the antitumor effect was further enhanced. Therefore, NP/mDs provide a promising strategy for the comprehensive treatment of malignancy.

1. Introduction

Training the host immune system to recognize biomimetic nanoformulations with natural camouflages has revolutionized recent prevention and therapy of malignancy [1–3]. By offering specific delivery, accurate recognition, professional presentation, and reliable immunostimulation, various platforms with unary or polynary biomembrane isolated from eukaryotes and prokaryotes have been developed to augment immunity [4–6]. Among them, mature dendritic cell (mDC)-derived dendrosomes, namely mDs, are emerging as a promising

modality, as the parent cells are classical sentinel antigen-presenting cells (APCs) that are able to initiate the cancer immunity cycle [7]. Because tumor-proximal DCs capture tumor antigen (TA) that is created and/or released during oncogenesis and oncology, they can secrete mDs with an inherited proteome, e.g., tumor antigen-major histocompatibility complexes (TA-MHC) and costimulatory molecules, which allows for strong immunostimulatory functionality as well [8,9]. Several mDs-based clinical trials have been conducted as cell-free cancer vaccines, showing the safety of these biovesicles, as well as the propensity to boost innate and adaptive immune systems of patients [10]. All the early

Peer review under responsibility of KeAi Communications Co., Ltd.

* Corresponding author. Department of Pharmaceutics, School of Pharmacy, Fudan University, Key Laboratory of Smart Drug Delivery, Ministry of Education, Shanghai, 201203, China.

** Corresponding author.

E-mail addresses: yinbo7@163.com (B. Yin), jxwang@fudan.edu.cn (J. Wang).

<https://doi.org/10.1016/j.bioactmat.2021.12.020>

Received 6 September 2021; Received in revised form 10 December 2021; Accepted 17 December 2021

Available online 21 December 2021

2452-199X/© 2021 The Authors. Publishing services by Elsevier B.V. on behalf of KeAi Communications Co. Ltd. This is an open access article under the CC BY-NC-ND license (<http://creativecommons.org/licenses/by-nc-nd/4.0/>).

testing of mDs monotherapy, however, has shown limited efficiency in patient cohorts with advanced malignancies [11]. This failure could be explained by insufficient allogeneic TA to drive the beneficial immune responses [7].

Given this, mDs-mediated TA-specific immunotherapy may be more effective as part of combinatorial treatment regimens. Immunogenic platinum (Pt) chemotherapeutics, such as oxaliplatin (OXA), have been challenging the traditional concept that cytotoxic agents are immunosuppressive and associated with tumor resistance and regrowth, and are identified as *in situ* stimuli that boost immune attack events in the dysfunctional tumor microenvironment (TME) [12,13]. This specific type of regulated cell death, defined as immunogenic cell death (ICD), is characterized by the chronic occurrence of damage-associated molecular patterns (DAMPs), e.g., the translocation of calreticulin (CRT) from the endoplasmic reticulum (ER) to cytomembrane, the pre-apoptotic exposure of heat shock proteins (Hsp) from stressed cells, the secretion of adenosine 5'-triphosphate (ATP) from stressed cells, and the cell death-associated release of nuclear high mobility group box 1 (HMGB1) [14–16]. Immunogenic chemotherapy with created autologous TA elicits robust innate and adaptive immune responses, with an increase in overall efficacy compared to cytotoxicity alone. Nevertheless, clinical practices using cytotoxic agents usually fail to meet requirements for effective treatment, mainly owing to severe side effects that result in decreased patient compliance. To address this issue, in the past several decades, nanoparticle (NP) technologies have made great strides in specific and efficient delivery of chemotherapeutics into tumors [17–20]. Armed with an adequate understanding of pathological abnormalities, e.g., the surge of redox potential in tumor tissues compared with that within normal tissues, bioresponsive polymers are appealing therapeutic platforms for the development of next-generation precision nano-medications [21].

Normally, immunocyte subpopulations are expected to detect and

eliminate derailed cells immediately, once APCs are recruited by the exposed TA. Cancers showing huge heterogeneity, however, evolve sophisticated strategies to evade immune recognition and attack. In particular, differentiated T cells are primary mediators of immune effector function, while the immune checkpoints maintaining immune homeostasis and preventing autoimmunity, are often inherently activated in the TME to suppress the nascent T lymphocyte response [22]. Recently, monoclonal antibody (mAb)-based immune checkpoint blockade therapies, such as PD-L1 mAb (α PD-L1), which unleash the final step of the immune cancer cycle, have yielded unprecedented results in clinical settings [23,24]. The excellent efficacy is probably attributed to their ability to reinvigorate unconstrained cytotoxic T lymphocytes (CTLs), which can maximize the potential to expand the breadth and magnitude of immune response.

Taking advantage of the biomimetic camouflages of dendrosomes, we succeeded in stuffing redox-responsive NPs into the cavity of mDs with personalized TA on the shell (Fig. 1). Poly(disulfide ester amide) (PDEA) polymers with disulfide spacers that readily reacted with thiols were synthesized and formulated with a family of OXA prodrugs having tunable hydrophobicity through the nanoprecipitation process to obtain OXA prodrug-loaded PDEA NPs, named as PO NPs. mDs with the natural ability to facilitate immunocyte-dependent tumor rejection were isolated from bone marrow-derived DCs, which were personalized with allogeneic TA in advance. NP/mDs with surface-expressing functional TA-MHC and costimulatory molecules, and core-swallowing immunogenic chemotherapeutics, were thus constructed by fusing NPs and mDs. Sonication and extrusion aided and promoted this process. *In vitro* and *in vivo* studies have reported that the NP/mDs with longer blood circulation and higher tumor accumulation could simultaneously interact with primary tumors and immunocytes to remodel the local TME: (1) the burst of redox-responsive NPs inside tumor cells converted dying cells into powerful immunogenic targets, which activated bystander DCs and

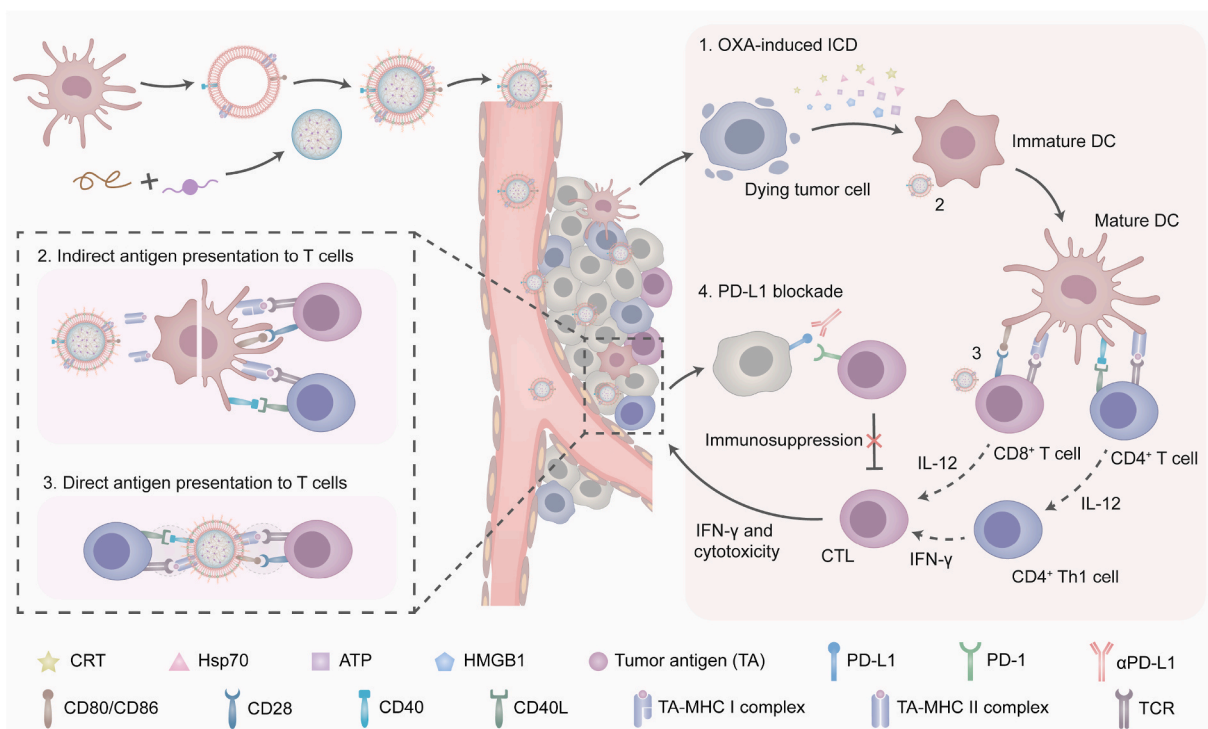


Fig. 1. Schematic illustration of NP/mDs interacting with primary tumors and immunocytes to remodel the local TME. The rapid burst of redox-responsive NPs inside tumor cells endowed dying cells with immunogenicity, which primed T cell response indirectly *via* bystander DCs. The camouflaged mDs transferred the trapped allogeneic TA to imDC surface for biometric recognition, a process termed cross-dressing. The last mechanism involved the presentation of allogeneic TA-MHC and costimulatory molecules on the surface of bioengineered NP/mDs, which gave them the potential to directly initiate immune response. Finally, the upregulated IL-12 and IFN- γ continued to break tolerance and license T cells to augment antitumor immunity. The blockade of PD-1/PD-L1 coupling unleashed host immunosuppression, resulting in the local regression of primary tumors and distant anti-metastasis of traveled tumors.

promoted TA-specific responses. (2) The trapped allogeneic TA was cross-dressed from mDs to imDC for biometric recognition. (3) The allogeneic TA-MHC and costimulatory molecules of mDs were directly presented to initiate lymphocyte differentiation. Subsequently, the upregulated IL-12 and IFN- γ that were secreted by lymphocytes continued to break tolerance and license T cells to augment antitumor immunity. Thus, NP/mDs could greatly sensitize the TME to PD-L1 blockade *via* immunogenic chemotherapy and TA-specific immunotherapy, leading to the local regression of primary tumors and distant anti-metastasis of traveled tumors. These findings have positive and potential implications for clinical translation of NP/mDs, and thus open a new avenue of therapeutic strategies for oncotherapy.

2. Experimental section

2.1. Preparation of PO12 NP-swallowed mDs (NP/mDs)

The biovesicle cloaking process was accomplished as previously reported with an optimized protocol [3,25]. PO12 NPs were dispersed and fused with mDs at an NP/protein mass ratio of 10:1 in the presence of DSPE-PEG2K (5.0 w/w%), followed by sonication in an ice-water bath for 5 min. The resulting NP/mDs were then successively extruded through 0.4, 0.2 and 0.1 μm polycarbonate membranes (Nuclepore Track-Etched Membranes, Whatman, UK) at room temperature using a LiposoFast-Basic & Stabilizer (Avestin, Canada) and stored at 4 °C until use.

Dil-hybrid NP/mDs (NP/Dil-mDs) were prepared by mixing predetermined amounts of PO12 NPs, mDs, DSPE-PEG2K, and dye (3.0 w/w% Dil), and then following the cloaking procedure as described above.

2.2. Protein composition analysis

The cytomembrane-associated proteins of mDCs were isolated with the Mem-PER Plus Membrane Protein Extraction Kit (89842, Thermo Fisher Scientific, USA). mDs, and NP/mDs were lysed with RIPA Lysis and Extraction Buffer (P0013C, Beyotime, China), supplemented with Protease Inhibitor Cocktail (P1010, Beyotime, China). The total protein concentration was determined using a Micro BCA Protein Assay Kit (23235, Thermo Fisher Scientific, USA) with a Hybrid Multi-Mode Reader.

Equal amounts of these denatured proteins were added to 10% SDS-polyacrylamide gels and separated using electrophoresis. The gels were stained with Colloidal Blue Staining Kit (PS111, EpiZyme, China).

2.3. Specific phenotype identification

The cytomembrane-associated proteins of imDCs, mDCs, mDs, and NP/mDs were isolated following the same protocol as described above and subjected to western blot analysis. Equal amounts of these denatured proteins were separated with 10% SDS-polyacrylamide gels and transferred to polyvinylidene fluoride (PVDF) membrane using electroblotting. The membranes were blocked with 5.0 w/w% Difco Skim Milk (BD, USA) in TBST at room temperature for 1 h, then incubated with CD40, CD80, CD86, and $\alpha 1 \text{ Na}^+/\text{K}^+$ ATPase primary antibodies (Abcam, USA), respectively, HRP-secondary antibodies (Abcam, USA), and Pierce ECL Plus Western Blotting Substrate (SQ201, EpiZyme, China). The blots were finally exposed on Amersham Hyperfilm ECL (GE Healthcare Life Sciences, USA) and band intensities of target proteins were analyzed using ImageJ.

2.4. Cell surface-exposed calreticulin (CRT) and heat shock protein 70 (Hsp70)

For the visualization of ICD markers, CT26 cells were seeded in 35 mm sterile glass bottom culture dishes (2×10^5 cells/dish) and

incubated with 1.0 mL of complete medium for 24 h. The cells were then treated with NP/mDs and each component for another 12 h. Afterward, the cells were incubated with Alexa Fluor 488-CRT antibody (Novus Biologicals, USA) and Alexa Fluor 647-Hsp70 antibody (Novus Biologicals, USA), respectively, and then counterstained with DAPI, and observed with a CLSM.

For the quantitative evaluation of ICD markers, CT26 cells were seeded in 6-well plates (2×10^5 cells/well) and incubated with 1.0 mL of complete medium for 24 h. The cells were then treated with NP/mDs and each component for another 12 h. Afterward, the cells were collected, incubated with Alexa Fluor 488-CRT antibody and Alexa Fluor 488-Hsp70 antibody (Novus Biologicals, USA), respectively, and then counterstained with PI, and analyzed using flow cytometry.

2.5. Extracellular adenosine 5'-triphosphate (ATP) and high mobility group box 1 (HMGB1)

CT26 cells were seeded in 6-well plates (2×10^5 cells/well) and incubated with 1.0 mL of complete medium for 24 h. The cells were then treated with NP/mDs and each component for another 24 h. Afterward, the cell supernatant was collected and extracellular ATP and HMGB1 concentrations were determined by ATP Determination Kit (A22066, Thermo Fisher Scientific, USA) and Mouse HMGB-1 ELISA Kit (E-EL-M0676c, Elabscience Biotechnology, China), respectively, according to the manufacturer protocols with a Hybrid Multi-Mode Reader.

2.6. imDC presentation after autologous TA engulfment

CT26 cells were seeded in 6-well plates (2×10^5 cells/well) and incubated with 1.0 mL of complete medium for 24 h. The cells were then treated with NP/mDs and each component for another 24 h and washed thrice with PBS. Afterward, the imDCs were cultured with the above pre-treated CT26 cells for 24 h before being incubated with CD16/CD32 antibody (Biolegend, USA) to reduce nonspecific binding to FcRs, and then APC-CD11c, FITC-CD80, and PE-CD86 antibodies (Biolegend, USA). The frequency of mDCs was analyzed using flow cytometry.

2.7. In vitro cross-dressing of biomembrane tracer

The lipophilic membrane stain, Dil, was used as a long-term tracer to investigate the transfer of biomembrane composition from NP/mDs to imDCs [26]. For the visualization of cross-dressing, imDCs were seeded in 35 mm sterile glass bottom culture dishes (5×10^5 cells/dish) and incubated with 1.0 mL of complete medium containing cytokines for 24 h. The cells were then treated with NP/Dil-mDs. At selected time intervals, the cells were washed thrice with PBS, counterstained with DAPI, and observed with a CLSM.

For the quantitative evaluation of cross-dressing, imDCs were seeded in 6-well plates (5×10^5 cells/well) and incubated with 1.0 mL of complete medium containing cytokines for 24 h. The cells were then treated with NP/Dil-mDs. At selected time intervals, the cells were collected, washed thrice with PBS, and analyzed using flow cytometry.

2.8. In vitro induction of imDC maturation

imDCs were seeded in 6-well plates (5×10^5 cells/well) and incubated with 1.0 mL of complete medium containing cytokines for 24 h. The cells were then treated with PBS, imDs, mDs, NP/mDs, and LPS for 24 h, washed thrice with PBS before being incubated with CD16/CD32 antibody, and then APC-CD11c, FITC-CD80, and PE-CD86 antibodies. The frequency of mDCs was analyzed using flow cytometry.

2.9. In vitro stimulation of lymphocyte proliferation and activation

Primary lymphocytes were isolated from spleens of healthy BALB/c mice by Mouse 1 \times Lymphocyte Separation Medium (7211011/

721101X, Dakewe Biotech, China) according to the manufacturer protocols. Briefly, BALB/c mice were sacrificed and the spleen was collected under aseptic condition. The tissue was ground with the rubber end of syringes and separated by the 70 μm cell filters. The splenocytes suspended in Lymphocyte Separation Medium were immediately transferred to a 15 mL centrifuge tube, covered with RPMI 1640 medium (1 mL), and centrifuged (800 g, 25 °C, 30 min). The lymphocyte layer was aspirated, re-suspended in RPMI1640 medium (10 mL), and centrifuged again to collect cells. The purified lymphocytes were seed in 96-well plates (3×10^5 cells/well) and incubated with 100 μL of complete medium for 24 h. The cells were then treated PBS, mDs, NP/mDs, and ConA for 72 h. Afterward, cellular proliferation was evaluated by Cell Counting Kit-8 (MA0218-2, Dalian Meilun Biotechnology, China) according to the manufacturer protocol with a Hybrid Multi-Mode Reader.

To evaluate the efficiency of lymphocyte activation, the purified lymphocytes were seeded in 24-well plates (1×10^6 cells/well) and incubated with 1.0 mL of complete medium for 24 h. The cells were then treated with PBS, mDs, NP/mDs, and ConA for 12 h, washed thrice with PBS before being incubated with CD16/CD32 antibody, and then PE-Cy7-CD3e, PE-CD8a, and APC-CD69 antibodies (Biolegend, USA). The frequency of CD8⁺CD69⁺ T cells was analyzed using flow cytometry.

2.10. *In vivo tumor suppression*

CT26 tumor-bearing BALB/c mice were randomly assigned into separate groups ($n = 6$ per group) and *i.v.* administrated with NP/mDs and each component at a Pt dose of 2.5 mg/kg, and/or *i.p.* injected with $\alpha\text{PD-L1}$ at a dose of 100 $\mu\text{g}/\text{mouse}$. Body weight, and other distress signs, such as rapid weight loss, dyspnea, mobility loss, inability to drink or feed, were monitored every other day. Tumor volume was measured using a digital caliper. After a Q3D \times 5 schedule, all mice were euthanized in accordance with institutional policy, and tumors were harvested, weighed, and imaged. Tumor inhibition rate (TIR) was calculated using the formula: $\text{TIR} (\%) = (W - W_s) / W \times 100$, where W is the average weight of tumors in PBS group and W_s is the weight of tumors in other groups.

2.11. *In vivo survival evaluation*

CT26 tumor-bearing BALB/c mice were randomly assigned into separate groups ($n = 6$ per group) and *i.v.* administrated with NP/mDs and each component at a Pt dose of 2.5 mg/kg, and/or *i.p.* injected with $\alpha\text{PD-L1}$ at a dose of 100 $\mu\text{g}/\text{mouse}$ for a Q3D \times 5 schedule. Body weight, distress signs, and tumor volume were monitored every other day. Mice were euthanized when they turned moribund according to pre-defined criteria in the protocol.

2.12. *Mitochondrial control of in vivo apoptosis*

CT26 tumor-bearing BALB/c mice were randomly assigned into separate groups ($n = 3$ per group) and *i.v.* administrated with NP/mDs and each component at a Pt dose of 2.5 mg/kg, and/or *i.p.* injected with $\alpha\text{PD-L1}$ at a dose of 100 $\mu\text{g}/\text{mouse}$. After a Q3D \times 5 schedule, all mice were euthanized in accordance with institutional policy, and tumors were collected and homogenized immediately with RIPA Lysis and Extraction Buffer, supplemented with Protease Inhibitor Cocktail and PMSF, using a tissue homogenizer. The total protein concentration was determined using a Micro BCA Protein Assay Kit and all samples were denatured by heating.

Western blot analysis was performed following the same protocol as described above, using p53, Bcl-2, caspase 3, and β -actin primary antibodies (Abcam, USA), respectively, and HRP-secondary antibodies (Abcam, USA).

2.13. *IF staining to label immunocytes*

CT26 tumor-bearing BALB/c mice were randomly assigned into separate groups ($n = 6$ per group) and *i.v.* administrated with NP/mDs and each component at a Pt dose of 2.5 mg/kg, and/or *i.p.* injected with $\alpha\text{PD-L1}$ at a dose of 100 $\mu\text{g}/\text{mouse}$. After a Q3D \times 5 schedule, all mice were euthanized in accordance with institutional policy, and tumors were collected and fixed immediately for IF staining.

The slides were retrieved, incubated with Alexa Fluor 647-CRT, Alexa Fluor 647-Hsp70, Alexa Fluor 594-CD4, Alexa Fluor 594-CD8a, Alexa Fluor 594-CD11c, Alexa Fluor 647-F4/80 antibodies (Novus Biologicals, USA), and FITC-CD3e antibodies (Invitrogen, USA), respectively, counterstained with DAPI before being observed with a Panoramic MIDI II Digital Slide Scanner.

2.14. *Flow cytometry to analyze tumor-infiltrating leukocytes*

CT26 tumor-bearing BALB/c mice were randomly assigned into separate groups ($n = 4$ per group) and *i.v.* administrated with NP/mDs and each component at a Pt dose of 2.5 mg/kg, and/or *i.p.* injected with $\alpha\text{PD-L1}$ at a dose of 100 $\mu\text{g}/\text{mouse}$. After a Q3D \times 5 schedule, all mice were euthanized in accordance with institutional policy, and tumors were harvested, cut into pieces, treated with collagenase IV, and ground with the rubber end of syringes.

Singlet suspensions were incubated with CD16/CD32 antibody, followed by incubation with PerCP Cy5.5-CD45, PE Cy7-CD3e, FITC-CD4, PE-CD8a, APC-CD25, PE-Foxp3, APC-CD11c, FITC-CD80, PE-CD86, FITC-F4/80, and APC-CD206 antibodies (Biolegend, USA), respectively. Cell populations were sorted using flow cytometry and data were analyzed using FlowJo X.

2.15. *Cytokine regulation*

CT26 tumor-bearing BALB/c mice were randomly assigned into separate groups ($n = 3$ per group) and *i.v.* administrated with NP/mDs and each component at a Pt dose of 2.5 mg/kg, and/or *i.p.* injected with $\alpha\text{PD-L1}$ at a dose of 100 $\mu\text{g}/\text{mouse}$. After a Q3D \times 5 schedule, all mice were euthanized in accordance with institutional policy, and tumors were harvested and homogenized following the same protocol as described above. The supernatants were collected for IL-12 and IFN- γ detection using QuantiCyto Mouse IL-12p70 ELISA kit and QuantiCyto Mouse IFN- γ ELISA kit (EMC006, EMC101g, Neobioscience, China), respectively, according to the manufacturer protocols.

2.16. *Antitumor vaccination*

CT26 cells were seeded in T75 flasks (1×10^7 cells/flask) and incubated with 10.0 mL of complete medium for 24 h. The cells were then treated with NP/mDs and each component for another 24 h, resulting in approximately 70% cell death. 1×10^6 dying CT26 cells suspended in 100 μL of RPMI 1640 medium-Matrigel Matrix mixture were *s.c.* implanted into the left flank of healthy BALB/c mice ($n = 6$ per group). One week later, those mice were re-challenged with 5×10^5 untreated CT26 cells on the contralateral flank. Tumor growth and incidence were monitored every other day. The absence of tumors was scored as an indication for efficient antitumor vaccination.

2.17. *Antitumor metastasis*

CT26 tumor-bearing BALB/c mice were randomly assigned into separate groups ($n = 5$ per group) and *i.v.* administrated with NP/mDs and each component at a Pt dose of 2.5 mg/kg, and/or *i.p.* injected with $\alpha\text{PD-L1}$ at a dose of 100 $\mu\text{g}/\text{mouse}$ for a Q3D \times 5 schedule. Three days later, those mice were *i.v.* infused with 5×10^5 untreated CT26 cells in 100 μL of PBS. Ten days later, all mice were euthanized in accordance with institutional policy, and lungs were collected and fixed with

Bouin's Fluid immediately.

Pulmonary metastasis subsequently appeared as yellow nodules on the lung surface, and nodule diameters of less than 0.5, 0.5–1, 1–2, and greater than 2 mm were classified as grade I, II, III, and IV, respectively. The total number of metastasis nodules (TNMN) was determined using the formula: $TNMN = (\text{the number of grade I}) + (\text{the number of grade II} \times 2) + (\text{the number of grade III} \times 3) + (\text{the number of grade IV} \times 4)$. The development of CT26 pulmonary metastasis nodules was also examined by H&E and Masson's trichrome staining.

2.18. Statistical analysis

All the graphs were made and statistical analyses were performed using GraphPad Prism 8. Two-sided unpaired Student's *t*-tests were used for comparisons between the means of two groups. For analysis of means of three or more groups, analysis of variance (ANOVA) tests were performed. In the event that ANOVA justified post hoc comparisons between group means, the comparisons were conducted using Tukey's multiple-comparisons tests. A Kaplan-Meier test was used for the survival rate and the data were statistically analyzed using log-rank (MantelCox) test. Statistical significance was set at $*p < 0.05$, $**p < 0.01$, $***p < 0.001$. The precise *P* values have been provided wherever possible and appropriate.

3. Results and discussion

3.1. The process of mDs swallowing NPs

The prodrug design of OXA has been applied with the aim to develop Pt derivatives with more favorable toxicity and tolerability profiles. Among them, OXA^{IV} prodrugs with inherently higher kinetic stability were the agents with potential clinical significance. The OXA^{IV} analogues were synthesized by mildly oxidizing OXA with H₂O₂, then reacting the intermediates with appropriate anhydrides to afford *trans*, *cis*, *cis*-bis(R)(oxalato)(1*R*,2*R*-cyclohexanediamine)Pt(IV), with R representing octoate (8), decanoate (10), dodecanoate (12), tetradecanoate (14), and hexadecanoate (16) (Fig. S1). Although the reaction condition of OXA8-16 was almost the same, the hydrophobicity of obtained OXA derivatives was varied by accurately regulating alkyl chain length. The detailed synthetic protocol and characterization are summarized in Figs. S2–6 and Table S1. Highly hydrophobic PDEA polymers were synthesized according to previous reports, *via* a one-step solution polycondensation of amino acids, diols, and dichlorides (Figs. S7–8) [27,28]. L-phenylalanine and sebacoyl chloride were chosen to mediate the intra/intermolecular interaction *via* hydrophobic force. Bis(2-hydroxyethyl) disulfide with disulfide bridges was used to regulate the polymer degradation in response to biological redox.

Given the importance of biointerfacing, the purposeful engineering of a solid NP that was suitable for natural membrane camouflage was considerable. Thus, various solid PO NPs were prepared by flash nanoprecipitation of PDEA polymers with OXA prodrugs. The effect of adjusting methylene linker length in OXA prodrugs on the particle size and Pt loading was fully evaluated. PO12 (OXA12-loaded PDEA) NPs with a diameter of 76.38 ± 1.06 nm and Pt loading of $8.83 \pm 1.24\%$ were identified as the most suitable candidate for the following biovesicle swallowing (Table S2). Moreover, it was found that as the hydrocarbon chain of OXA prodrugs increased, the particle size of corresponding NPs systematically increased from 66.06 ± 0.46 to 127.73 ± 0.75 nm, as measured by dynamic light scattering (DLS). Meanwhile, the Pt loading increased with increasing hydrocarbon chain at first, but then decreased if the number of methylene spacer were higher than 10. Thus, the modification of OXA with different hydrophobic chains could precisely regulate the physicochemical properties of NPs. Electrophoretic light scattering (ELS) also revealed that all PO NPs exhibited negative surface zeta potentials ranging from -7.69 to -0.32 mV. Rhodamine 6G-loaded PO12 NPs (Rd-PO12 NPs), Coumarin 6 and Nile red-loaded PO12 NPs

(CN-PO12 NPs), and DiR-loaded PO12 NPs (DiR-PO12 NPs) were prepared similarly with the above dye introduced during nanoprecipitation.

With the provision of granulocyte-macrophage colony-stimulating factor (GM-CSF) and interleukin-4 (IL-4), hematopoietic bone marrow progenitor cells that were collected from healthy rodents initially transformed into immature DCs (imDCs), which were characterized by high endocytic activity and low T cell activation potential [29]. Those imDCs subsequently sampled the surrounding environment for CT26 TA and lipopolysaccharide (LPS), and finally were activated into mDCs with multiple pseudopodia (Fig. S9). The stimulation of imDCs with TA could serve a dual purpose, not only facilitating maturation to circumvent immune tolerance but also capturing specific antigen to manipulate immune responses. Cytochalasin B was used to bind the fast-growing end of F-actin to block the microfilament polymerization, which affected the membrane rigidity of mDCs and contributed to the release of nano-sized mature dendrosomes, namely mDs (Fig. S10) [25,30].

The fabrication process of NP/mDs is illustrated in Fig. 2a. mDs-camouflaged PO12 NPs, denoted as NP/mDs, were engineered by fusing mDs, NPs, and 1,2-distearoyl-*sn*-glycero-3-phosphoethanolamine-*N*-[methoxy(polyethylene glycol)-2000] (ammonium salt) (DSPE-PEG2K) at an optimized ratio. Physical sonication and extrusion steps were used to induce the membrane swallowing process, which ultimately resulted in the desired NPs with the particle size of 91.24 ± 0.78 nm, zeta potential of -17.77 ± 1.50 mV, Pt loading capability of $6.91 \pm 1.42\%$, and spherical shape with core-shell structure, observed under Transmission Electron Microscopy (TEM) (Fig. 2b–d and S11, Table S2). Improved colloidal stability was measured for both bare NPs and NP/mDs, which was attributable to the stabilizing effect of polyvinyl alcohol and high surface charge of the outer membrane (Fig. S12).

It was hypothesized that the intracellular redox-responsive process of NP/mDs with a high density of disulfide groups could achieve specific tumor-killing effect. TEM was utilized to monitor *in vitro* disintegration of PO12 NPs and NP/mDs in response to dithiothreitol (DTT) (Fig. S13). As time prolonged, the spherical structure of nanoplateforms was rapidly degraded into irregular debris. The release kinetics under gradient redox mediums, mimicking biofluids, was carried out and the released Pt was measured by Inductively Coupled Plasma-Mass Spectrometry (ICP-MS). As shown in Fig. 2f and S14, for NP/mDs incubated with PBS, less than 20% of total Pt payloads was released over the course of 72 h, indicating the platform could avoid burst release of Pt. However, within the same intervals, approximately 40% and 80% of the charged Pt were detected by incubating in 1 and 10 mM DTT solution, respectively, demonstrating the reduction-promoted disassembly of PDEA polymers with concomitant release of entrapped drugs. PO12 NPs without biomembrane camouflages had obviously accelerated release patterns, particularly in a high reducing medium. In stark contrast, OXA12-loaded PLGA NPs delivered drugs with a lengthy delay. DTT with the maximum concentration led to less than 30% of Pt released from nonresponsive PLGA polymers within three days. These results provided a sufficient evidence that PDEA polymers governed the redox-sensitivity in the platform.

We hypothesized that various cytomembrane-associated proteins were still present on the artificial biovesicles, thus reserving the essential immunostimulatory faculties of parent cells. The membrane protein composition of mDCs, mDs, and NP/mDs was investigated by sodium dodecyl sulfate-polyacrylamide gel electrophoresis (SDS-PAGE) to compare their biomarker fingerprints (Fig. 2e). It could be found that mDs-camouflaged PO12 NPs inherited a complete proteinogram from donor cells, maximizing the likelihood of TA-specific delivery. Analysis of the whole band intensity also reflected that the manufacturing process of NP/mDs exerted little impact on the constituent and structure of proteins. CD40, CD80, and CD86, immune-associated costimulatory molecules of mDCs, are typical membrane proteins directly involved in the priming and activation of effector T cells. To identify these specific phenotypes, western blots of membrane proteins of imDCs, mDCs, mDs, and NP/mDs were conducted (Fig. 2g and S15). The presence and expression of CD40, CD80, and CD86 in NP/mDs were almost identical

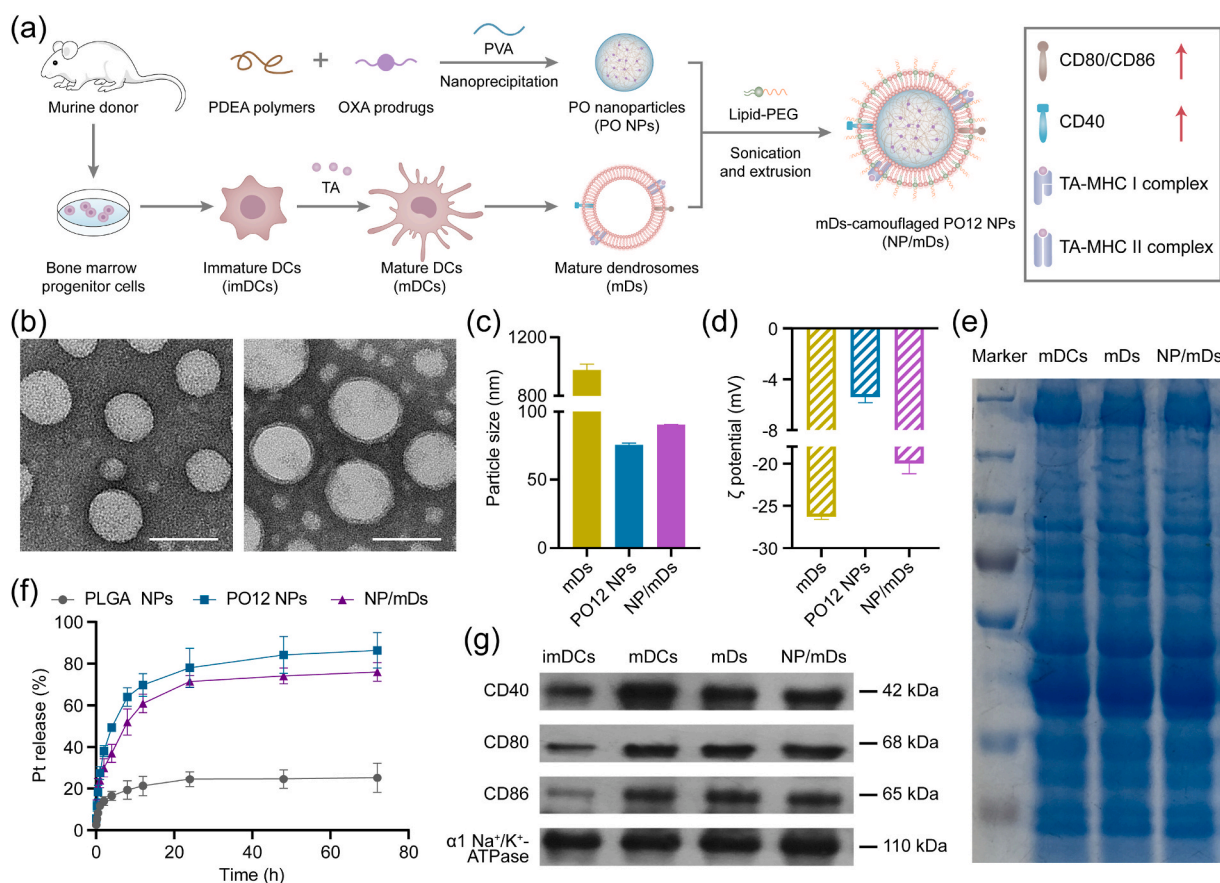


Fig. 2. Characterization of NP/mDs. (a) Schematic illustration for the nanoprecipitation of PO NPs, the isolation of mDs, and the cloaking of NP/mDs. (b) Typical TEM images of PO12 NPs and NP/mDs. Scale bar = 100 nm. (c) Particle size and (d) zeta potential (ξ) of mDs, PO12 NPs, and NP/mDs, $n = 3$. (e) SDS-PAGE pattern of cytomembrane-associated proteins isolated from mDCs, mDs, and NP/mDs. (f) *In vitro* release profiles of Pt from PLGA NPs, PO12 NPs, and NP/mDs in 10 mM DTT at 37 °C, $n = 3$. (g) Western blot assay of CD40, CD80, and CD86 in cytomembrane-associated proteins extracted from imDCs, mDCs, mDs, and NP/mDs. $\alpha 1$ Na⁺/K⁺ ATPase was used as the loading control. Data points in c, d, and f represent mean \pm SD.

between mDCs and mDs, while the apparent loss of the above markers was detected in imDCs. These results confirmed that the trapped TA promoted the terminal maturation of murine DCs, and NP/mDs assembled by physical fusion reserved the immunomodulatory potential of parent cells.

3.2. NP/mDs engaged in immunogenic chemotherapy *in vitro*

Next, we evaluated cellular internalization of NPs and NP/mDs by using Rhodamine 6G (Rd) as a fluorescent probe (Fig. 3a and S16). Flow cytometry analysis showed that NPs with or without mDs cloaking were all internalized into tumor cells in a time-dependent manner. Interestingly, the camouflages with mDs slightly increased the uptake efficiency of NPs. This might be attributed to the possession of cell-originating lipid bilayers, which could fuse with the membrane of accessible cells, thus promoting the accumulation of trackers inside tumor cells. Intracellular disintegration through disulfide-mediated redox was validated by Förster resonance energy transfer (FRET). As seen in Fig. 3b and S17, the donor, Coumarin 6, excited with 410 nm, transferred energy to the closest proximal acceptor, Nile red, within 4 h, resulting in a typical FRET signal. Once the platform disassembled inside CT26 cells, the separation of FRET pairs (>10 nm) resulted in the decrease of non-radiative dipole-dipole coupling, halting the acceptor emission, leading to an observed loss of red fluorescence. However, once tumor cells were pre-exposed to N-ethylmaleimide (NEM, an irreversible thiol-exhauster), persistent FRET imaging was captured under Confocal Laser Scanning Microscope (CLSM). These results further confirmed the intracellular redox-triggered disintegration of our system.

The direct cytotoxicity of NP/mDs against CT26 cells was examined. PDEA NPs (control NPs) were prepared but in the absence of OXA12. Cellular viability is shown in Fig. 3c and S18, and EC₅₀ results are listed in Table S3. Compared with free components and control NPs that displayed limited toxicity to tumor cells, NP/mDs showed the lowest EC₅₀ values ($8.86 \pm 2.52 \mu\text{M}$ at 48 h and $4.30 \pm 0.48 \mu\text{M}$ at 72 h) across the tested intervals. Subsequently, apoptosis with Annexin V-FITC and PI double staining was conducted to detect the translocation of membrane phosphatidylserine (PS) from the inner face of the plasma membrane to the outer surface (Fig. 3d and S19). Flow cytometry analysis showed that all treatment groups containing OXA or OXA prodrugs enhanced apoptosis significantly, among which NP/mDs showed the strongest effect to induce the percentages of apoptotic and necrotic cells from $7.63 \pm 0.16\%$ to $41.23 \pm 0.96\%$.

Since OXA can induce tumor apoptosis with the emission of immunogenic DAMPs [31], we assessed ICD markers, including CRT, Hsp70, ATP, and HMGB1. As seen in Fig. 3e and S20-21, among all treatment groups, a highest level of CRT translocation from the lumen of ER to the surface of dying cells was observed by immunofluorescence (IF) staining for CT26 cells treated with NP/mDs, indicating they were outputting the strongest “eat me” signals. The expression of another important surface-exposed marker, Hsp70 (a DC maturation promotor), was also obviously upregulated after CT26 cells were incubated with NP/mDs. HMGB1 expelled from dying cells to extracellular milieu for APC presentation is considered to be a marker of late ICD. As shown in Fig. 3f, NP/mDs displayed a 1.81-fold increase in the discharged HMGB1 compared with supernatants collected from the PBS group. Further, based on the detection of ATP (an important “find-me” signal for

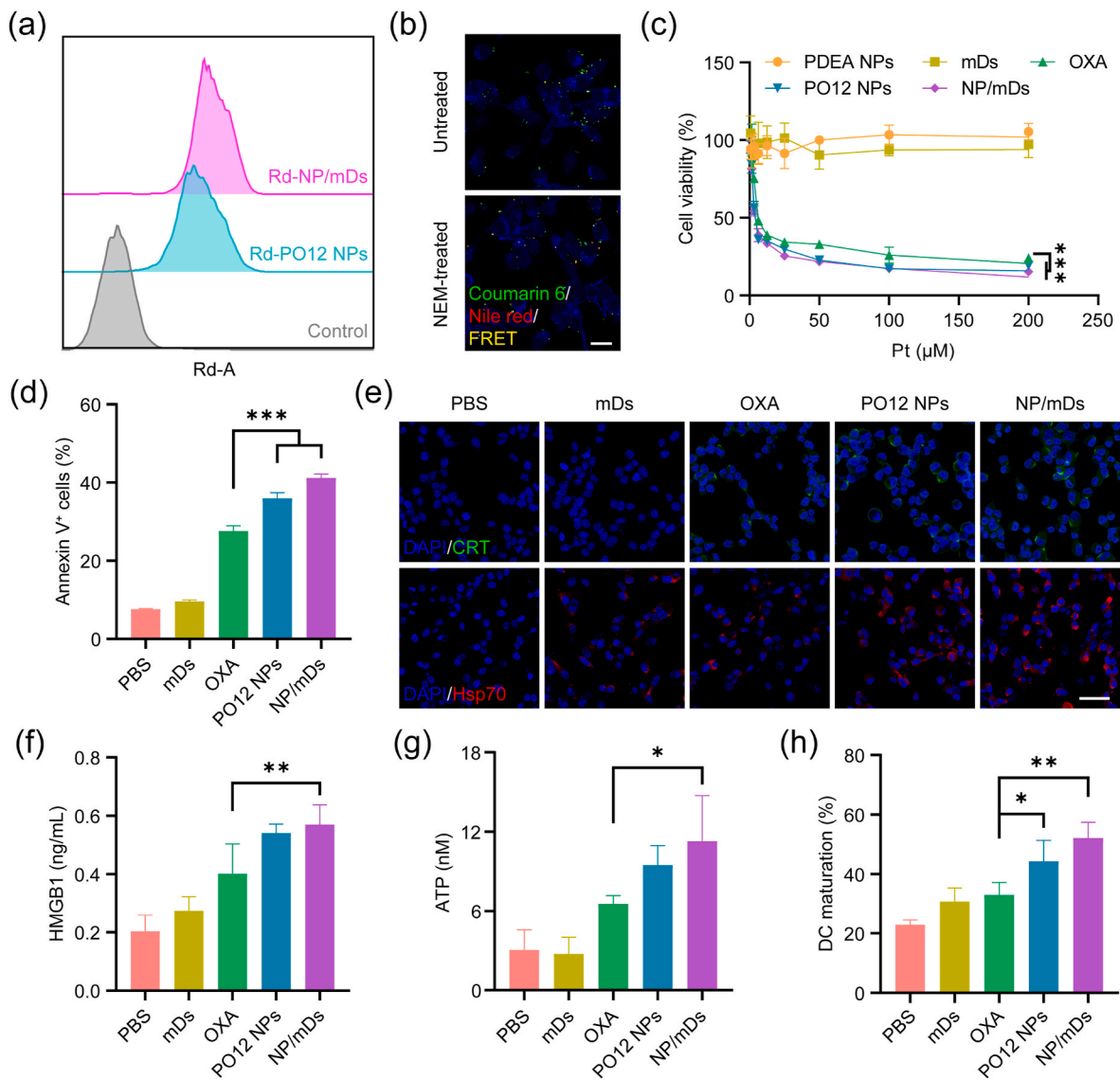


Fig. 3. NP/mDs engaged in immunogenic chemotherapy *in vitro*. (a) Histogram analysis of *in vitro* cellular uptake of Rd-PO12 NPs and Rd-NP/mDs at 1 h. (b) CLSM images of CT26 cells after incubating with CN-NP/mDs for 8 h. N-ethylmaleimide (NEM) was used to consume intracellular sulfhydryl. The visualization of cells was achieved by Hoechst 33342 staining. Scale bar = 20 μm. (c) The cytotoxicity of CT26 cells after treatment with NP/mDs and each component for 72 h, n = 3. OXA had significant differences in EC₅₀ values with PO12 NPs and NP/mDs. (d) *In vitro* apoptosis of CT26 cells treated with NP/mDs and each component for 24 h, n = 3. (e) CRT translocation and Hsp70 exposure to outer plasma membrane of CT26 cells after incubating with NP/mDs and each component for 12 h. Scale bar = 50 μm. (f) HMGB1 release and (g) ATP secretion from CT26 cells after incubating with NP/mDs and each component for 24 h, n = 3. (h) The engulfment of ICD-induced TA from dying tumor cells by imDCs, n = 3. Data points in c, d, f, g, and h represent mean ± SD. Statistical significance was calculated by ANOVA with Tukey's test. n.s., not significant, **p* < 0.05, ***p* < 0.01, and ****p* < 0.001.

phagocytes) in the extracellular fluid, NP/mDs enhanced ATP externalization by 3.71-fold over PBS control (Fig. 3g). The ICD concept is defined as a unique approach of regulated cell death emitting a set of endogenous molecules with immunogenic competence to interact with innate immunocytes for activation and maturation, which enables a complete antigen-specific adaptive immune response [32]. Therefore, after treatment with NP/mDs and controls, the dying CT26 cells were washed carefully and cultured with imDCs, using CD11c, CD80, and CD86 as markers to evaluate DC maturation. The data presented in Fig. 3h and S22 revealed that the percentage of mDCs in the NP/mDs group ($52.17 \pm 5.26\%$) was significantly higher than other groups ranging from 22.90% to 44.33%, indicating the presentation of bystander DCs after engulfment of extracellularly autologous TA exposed by immunogenic chemotherapy.

3.3. NP/mDs elicited TA-specific immune response *in vitro*

Since mDC-derived vesicles can indirectly or directly present surface TA to T cells [7], the immunoresponse capacity of NP/mDs was studied. The cytotoxicity of NP/mDs against imDCs (>80% cell viability across tested concentrations) did not present statistical significance at EC₅₀ values of tumor cells, likely owing to intracellular redox difference between CT26 cells and normal imDCs (Fig. 4a). Apart from ICD, the second mechanism by which NP/mDs may boost immunization is a process known as cross-dressing [26,33]. In this process, NP/mDs merged with the surface membrane of accessible imDCs, thereby transferring their intact TA-MHC for cognate T cell presentation without processing [34,35]. To explore this possibility, the membrane transferring course between donor NP/mDs and acceptor imDCs was evaluated using a lipophilic membrane stain, Dil, as a long-term tracer [26]. The dye is weakly fluorescent until incorporated into membranes.

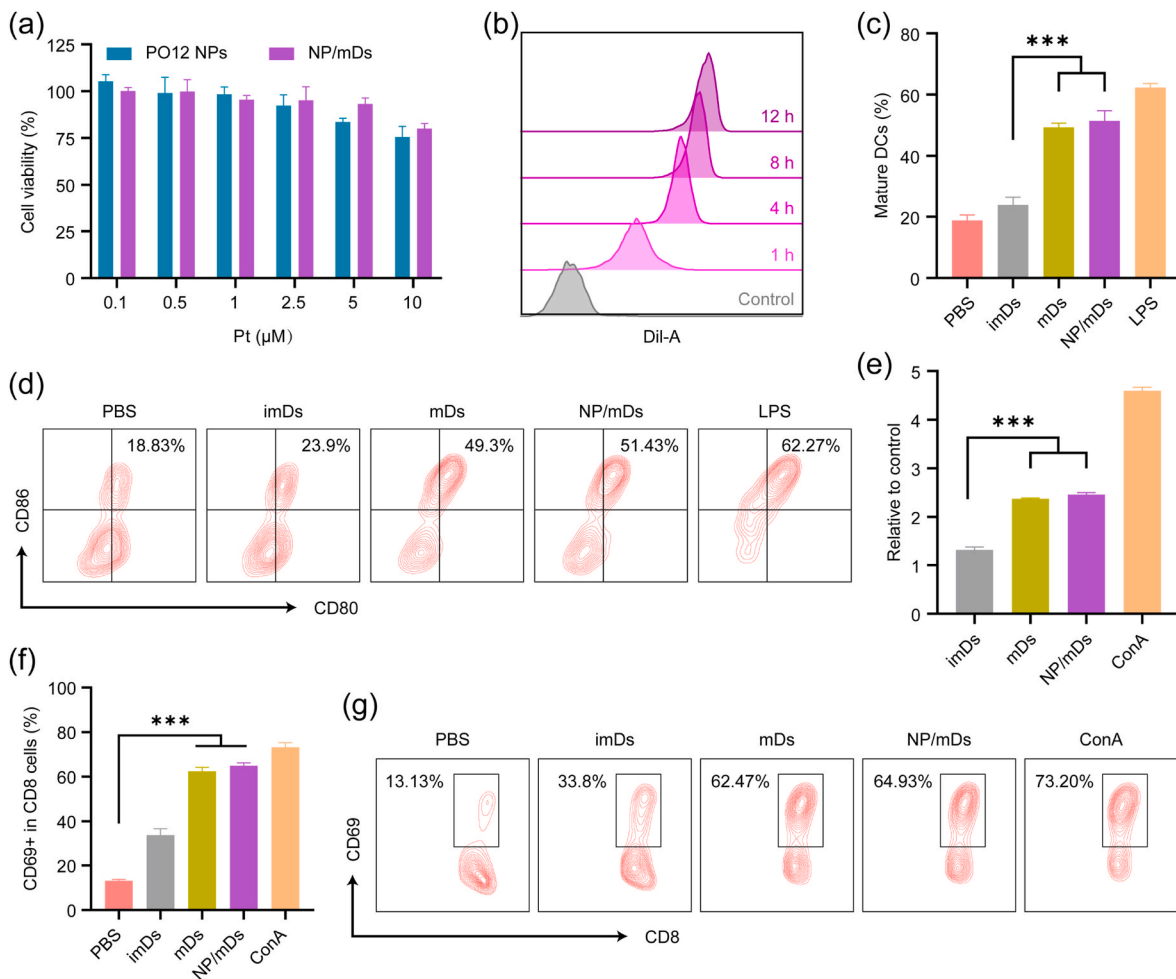


Fig. 4. NP/mDs elicited TA-specific immune response *in vitro*. (a) The viability of imDCs treated with PO12 NPs and NP/mDs for 72 h, $n = 3$. (b) Histogram analysis of *in vitro* NP/Dil-mDs to imDCs cross-dressing of biomembrane tracer. (c) *In vitro* induction of imDC maturation by NP/mDs, $n = 3$. LPS treatment served as a positive control, while PBS was negative. (d) Representative flow cytometry plots for gating mature DCs. (e) *In vitro* stimulation of lymphocyte proliferation, $n = 3$. ConA treatment served as a positive control. (f) *In vitro* activation of T lymphocyte, $n = 3$. (g) Representative flow cytometry plots for gating CD8⁺CD69⁺ T cells. Data points in a, c, e and f represent mean \pm SD. Statistical significance was calculated by ANOVA with Tukey's test. n.s., not significant, * $p < 0.05$, ** $p < 0.01$, and *** $p < 0.001$.

imDCs were incubated with NP/Dil-mDs for different lengths of time. CLSM showed that the red fluorescent signal on the surface of imDCs, an index of biomembrane composition transfer, increased with time in 12 h (Fig. S23a). Flow cytometry analysis proved that feeding NP/Dil-mDs to imDCs resulted in the detection of increased Dil signal from cells over time, validating the likelihood that imDCs could pillage membrane components from neighboring NP/mDs by cross-dressing (Fig. 4b and S23b).

To further investigate whether cross-dressing was the means by which imDCs picked up TA from NP/mDs to initiate the subsequent antitumor response, several typical phenotypes (e.g., CD11c, CD80, CD86), were measured to identify the nature and evolution of DC maturation state (Fig. 4c and d). Unlike imDs (immature dendrosomes), mDs with trapped allogeneic TA after incubating with imDCs significantly increased the percentage of CD80⁺CD86⁺ DCs ($49.30 \pm 1.42\%$ vs. $18.83 \pm 1.72\%$ for PBS), a response similar to that of LPS-stimulation ($62.27 \pm 1.35\%$). Consistent with their camouflages, NP/mDs had the full capacity to stimulate the differentiation of imDCs ($51.43 \pm 3.33\%$), supporting the hypothesis that the complete cross-dressing chain served as an effective mode to transfer preformed and unprocessed TA-MHC between NP/mDs and imDCs.

The third possible route through which NP/mDs prime T cell response is occur *via* the direct presentation of TA-MHC and additional

costimulatory molecules, and it appeared that this mechanism operated most efficiently as a restimulation of T cells [36,37]. In support of this paradigm, primary lymphocytes were isolated from the spleen of BABL/c mice and treated with imDs, mDs, NP/mDs, and concanavalin A (ConA, a T lymphocyte division initiator). As shown in Fig. 4e, the proliferation rates of mDs and NP/mDs were 2.37- and 2.46-fold higher than PBS, respectively, but indistinctly occurred in imDs (1.31-fold over PBS) group, indicating that mDs could effectively stimulate the proliferation of T cells. CD69 is an early marker of T cell activation, as shown in Fig. 4f and g, significant levels of T lymphocyte activation similar to ConA (5.57-fold over PBS) treatment was obtained in mDs (4.94-fold over PBS) and NP/mDs (4.76-fold over PBS) groups, indicating that NP/mDs-to-T cell stimulation appeared to be efficient in creating effector lymphocytes *via* a mechanism that required direct contact only.

Hence, all *in vitro* results suggested that the redox-sensitive NPs camouflaged with mDs potentially converted tumor cells into powerful immunogenic targets, benefited DC maturation from cross-dressing mechanism, as well as allowed immediate antigen presentation from the cloaking membrane to T cells.

3.4. Artificial camouflages endowed NP/mDs with longer circulation and higher penetration

Pharmacokinetic (PK) behaviors of SD rats undergoing a single bolus intravenous (*i.v.*) administration of OXA, PO12 NPs, and NP/mDs were investigated by using Pt as a real-time tracer. As shown in Fig. 5a, free OXA showed a Pt curve presenting rapid elimination, while PO12 NPs and NP/mDs exhibited significantly stable and mild decline profiles, showing that nanomedicines offered longer blood retention time. In fitting classical compartment models to empirical data, it was found that the two-compartment model with first-order distribution and elimination processes, $C(t) = A \cdot e^{-\alpha t} + B \cdot e^{-\beta t}$, fit the plasma concentration-time curves best, and PK parameters calculated with WinNonlin are summarized in Table S4. The comparison of hybrid constants and first-order rate constants among groups confirmed that both distribution and elimination phases of PO12 NPs and NP/mDs decreased in much more mild patterns, a sign of drug enrichment in the central compartment. Analysis of plasma half-life indexes further concluded that PO12 NPs (0.52 ± 0.10 h for $t_{1/2\alpha}$ and 11.82 ± 3.82 h for $t_{1/2\beta}$) and NP/mDs (0.92 ± 0.27 h for $t_{1/2\alpha}$ and 15.93 ± 5.94 h for $t_{1/2\beta}$) greatly prolonged Pt circulation in the general system as compared with free OXA (0.19 ± 0.04 h for $t_{1/2\alpha}$ and 2.67 ± 0.72 h for $t_{1/2\beta}$). Additionally, the non-compartmental model based on statistical moment theory was performed for bioequivalence evaluation. $AUC_{0 \rightarrow \infty}$ and $AUMC_{0 \rightarrow \infty}$ values for Pt were increased by 11.27- and 49.71-fold, respectively, after encapsulation into NP/mDs. The enhanced bioavailability was supported by significantly reduced CL (0.02 ± 0.01 L/(h·kg) for NP/mDs vs.

0.22 ± 0.07 L/(h·kg) for PBS). $MRT_{0 \rightarrow \infty}$ parameters of PO12 NPs and NP/mDs were significantly extended over free drugs by 3.34- and 4.18-fold, respectively, suggesting prolonged blood circulation. The V_{ss} at steady state of NP/mDs was decreased by 65.09%, indicating limited tissue distribution.

Next, tumor accumulation capacity of NP/mDs was evaluated by *in vivo* near-infrared (NIR) imaging using DiR as the fluorescent probe. As recorded in Fig. 5b, the real-time NIR signal of DiR-NP/mDs in tumor sites could be captured 8 h after injection, and the fluorescence increased with time and reached a maximum at 24 h. In contrast, almost no signal in tumors was observed from the free probe group within 24 h imaging, illustrating the tumor enrichment and biofluid retention abilities of NP/mDs. Then, all mice were euthanized by CO₂ suffocation and *ex vivo* tissue imaging was performed (Fig. 5c–d and S24). For the mice dosed with DiR-PO12 NPs and DiR-NP/mDs, the pronounced NIR signal from tumors and plasma accounted for more than 40% of the total fluorescence detected. Subsequently, all solid tissues were embedded in paraffin and cut into slides with microvessels stained with CD31 antibody and nuclei stained with DAPI. As displayed in Fig. 5e and S25, NP/mDs primarily bypassed the mononuclear phagocytic system (MPS) and effectively reduced the probe distribution to off-target organs. Importantly, in tumor sections of DiR-NP/mDs, DiR fluorescent signals were observed at the highest level and co-localized to tumor neovascular lumens, confirming the enrichment behaviors in solid tumors.

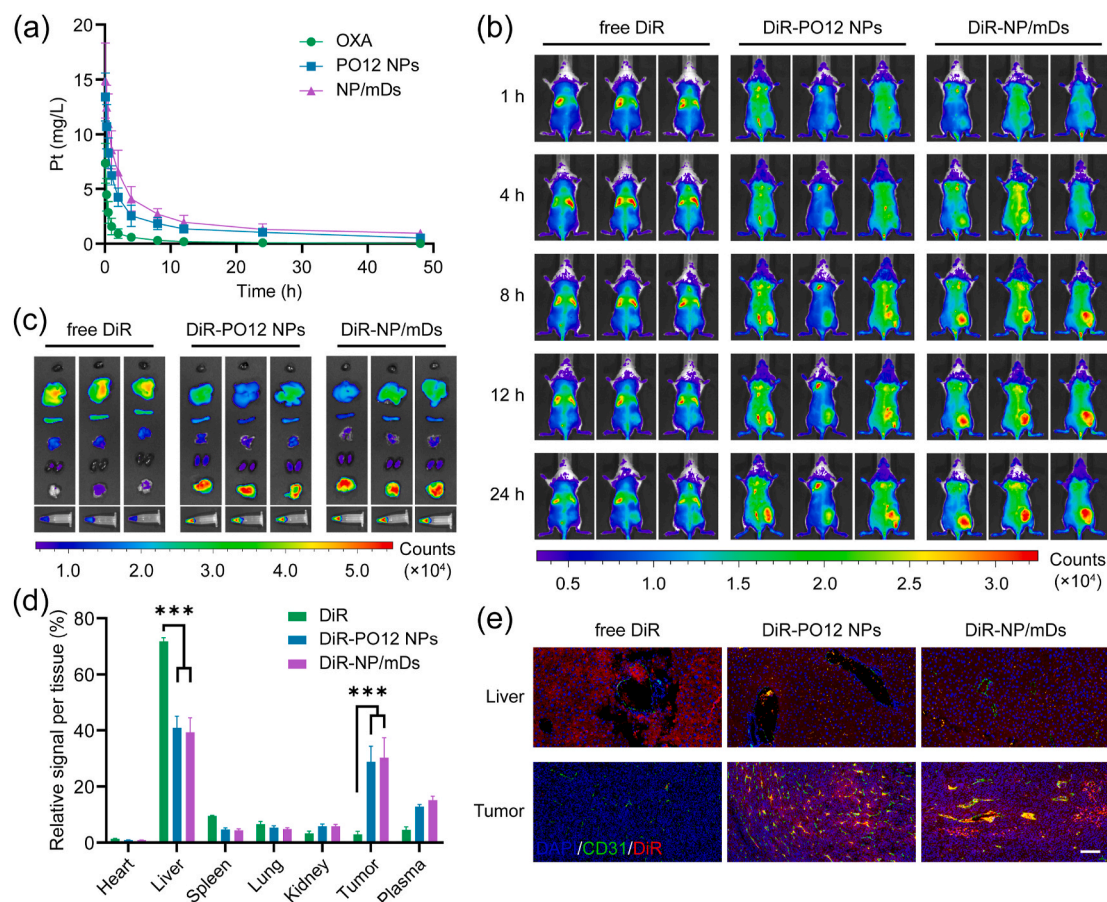


Fig. 5. *In vivo* trafficking of NP/mDs. (a) Time-dependent Pt profiles in the blood after an *i.v.* dose of OXA, PO12 NPs, and NP/mDs to SD rats, $n = 3$. (b) Time-lapse NIR fluorescent imaging of BALB/c mice bearing CT26 syngeneic tumors after an *i.v.* injection of free DiR, DiR-PO12 NPs, and DiR-NP/mDs, $n = 3$. (c) *Ex vivo* NIR imaging of resected organs, tumors, and plasma. (d) The quantitative biodistribution analysis based on the total NIR signals. (e) The co-localization of free DiR, DiR-PO12 NPs, and DiR-NP/mDs in liver and tumor with microvessels stained with CD31 antibody and nuclei stained with DAPI. Scale bar = 100 μ m. Data points in a and d represent mean \pm SD. Statistical significance was calculated by ANOVA with Tukey's test. n.s., not significant, * $p < 0.05$, ** $p < 0.01$, and *** $p < 0.001$.

3.5. Systemic therapy with NP/mDs inhibited primary tumor growth

The maximum tolerated dosage (MTD) of NP/mDs in healthy BALB/c mice was explored in a study of increasing doses of 0.5, 1.5, 2.5, 3.5, and 4.5 mg Pt/kg (Fig. S26). It was clear that those mice receiving a dose at 3.5 and 4.5 mg Pt/kg showed rapid weight loss or death. All other animals, however, tolerated *i.v.* administration of NP/mDs without any distress signs. Thus, the MTD of NP/mDs could be inferred to be 2.5 mg Pt/kg for following tests. Implementation of Pt-based chemotherapy is challenging to practice in clinical settings, mainly owing to the large range of side effects, such as myelosuppression and organ damage that occur acutely and chronically [38,39]. Complete blood count and biochemical analysis provide a more accurate assessment of dose related side effects than weight loss or distress symptoms. The blood panel of healthy BALB/c mice undergoing five cyclic treatments with NP/mDs, each component of NP/mDs, and NP/mDs with α PD-L1 with three-day intervals (Q3D) are listed in Tables S5–6. OXA, known to cause harsh neutropenia, reduced WBC (2.0 ± 0.7 vs. 4.5 ± 1.2 ($10^9/L$) for PBS), GRA (0.6 ± 0.3 vs. 1.8 ± 0.3 ($10^9/L$) for PBS), and PLT (581 ± 174 vs. 915 ± 114 ($10^9/L$) for PBS) significantly, while NP/mDs and the others displayed negligible effect on mouse hemogram. Furthermore, a slight and occasional increase in ALT, AST, and CREA was only found for the mice administered with free OXA, implying its potential risk for developing hepatotoxicity and nephrotoxicity.

To validate *in vivo* antitumor efficacy, CT26 tumor-bearing BALB/c mice were established and *i.v.* administrated with NP/mDs and each component, and/or intraperitoneally (*i.p.*) injected with α PD-L1 in a Q3D \times 5 schedule (Fig. 6a). The tumor volumes of PBS and α PD-L1

groups grew sharply throughout the observation period, while the tumor growth profiles of mDs, OXA, PO12 NPs, and NP/mDs groups were controlled to some extent. In comparison, the mice dosed with NP/mDs and α PD-L1 could inhibit tumor growth significantly, which developed primary tumors with average volumes of 0.27 ± 0.16 cm³ on day 21 post tumor engraftment, revealing a significant synergistic effect (Fig. 6b and S27a). Tumor inhibition rate (TIR) of the combination therapy was found to be $81.01 \pm 7.71\%$, significantly greater than the recorded TIRs of $38.18 \pm 12.73\%$ for mDs, $45.19 \pm 9.56\%$ for OXA, $58.97 \pm 11.27\%$ for PO12 NPs, and $68.66 \pm 8.78\%$ for NP/mDs, consistent with the harvested tumor images (Fig. 6c). In addition, the slight weight loss induced by OXA monotherapy over the duration was exempted in other groups, indicating combination therapy was able to not only suppress local tumor growth but also alleviate serious side effects (Fig. S27b).

Survival analysis of NP/mDs and their combination with α PD-L1 in a Q3D \times 5 schedule was subsequently evaluated (Fig. 6d and e and Table S7). The mice were euthanized if either the tumor size reached the human endpoint or serious distress signs were observed. Of the individuals dosed with PBS and α PD-L1, the median survival was less than 23 days. However, *i.v.* injection with mDs, OXA, and PO12 NPs slightly increased this time to 27, 30, and 34 days, respectively. NP/mDs greatly extended median survival to 38 days. In stark contrast, the combination of NP/mDs and α PD-L1 maximally suppressed the growth of CT26 syngeneic tumors for up to 44 days, a remarkable achievement in altering the natural progress of murine colon cancer (Fig. S28). The results demonstrated that NP/mDs could generate foreign and apoptotic antigen *in situ*, facilitate the engulfment and presentation of APCs, and participate in the immunological decision to mount T cell response,

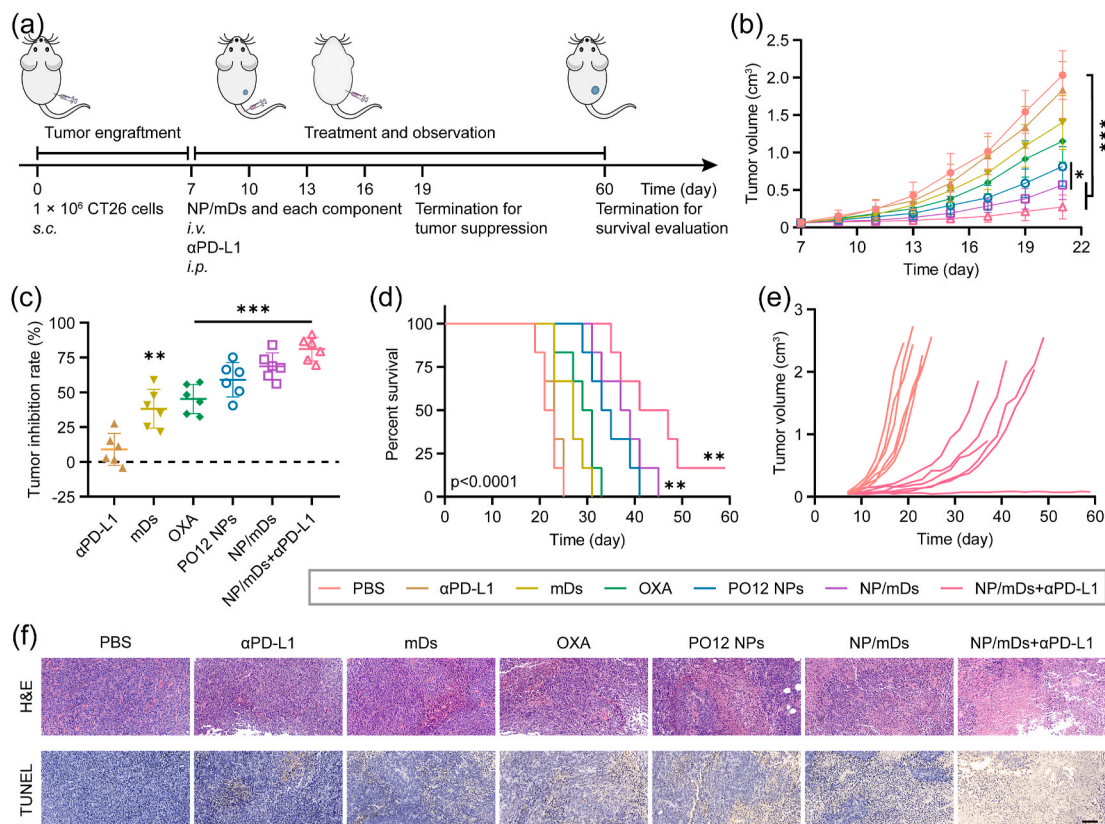


Fig. 6. Systemic therapy with NP/mDs inhibited primary tumor growth. (a) Schematic representation of CT26 tumor engraftment and treatment in BALB/c mice for tumor suppression and survival evaluation. (b) Tumor growth profiles for CT26 tumor-bearing BALB/c mice *i.v.* injected with NP/mDs and each component, and/or *i.p.* injected with α PD-L1 in a Q3D \times 5 schedule, $n = 6$. (c) Tumor inhibition rates of CT26 tumor-bearing BALB/c mice over the course of Q3D \times 5 chemotherapy and/or immunotherapy. (d) Kaplan-Meier survival curves of CT26 tumor-bearing BALB/c mice during survival evaluation, $n = 6$. (e) Individual tumor growth curves for CT26 tumor-bearing BALB/c mice in PBS and NP/mDs+ α PD-L1 groups during survival evaluation. (f) *Ex vivo* tumor sections with H&E and TUNEL staining. Scale bar = 100 μ m. Data points in b and c represent mean \pm SD. Statistical significance was calculated by ANOVA with Tukey's test. n.s., not significant, * $p < 0.05$, ** $p < 0.01$, and *** $p < 0.001$.

whereas the blockade of PD-1/PD-L1 interaction, known to drive T cell dysfunction, might be the key to unleash the antitumor immunity.

Histopathology of organs and tumors harvested from CT26 tumor-bearing BALB/c mice was assessed using hematoxylin and eosin (H&E) staining (Fig. 6f and S29). Pathological evaluation demonstrated no obvious changes in any organs harvested from PBS, α PD-L1, mDs, PO12 NPs, NP/mDs, and NP/mDs+ α PD-L1 groups. The mice undergoing free OXA treatment, however, presented some typical organ damage, e. g., liver injury with hyperemia and vacuolar degeneration, incomplete spleen structure, and swelled glomeruli with hydropic degeneration. Upon the termination of regimen, tumors harvested from mDs and chemotherapy groups displayed fragmented and/or shrunken cellular morphology with concentrated chromatin, indicating tumor necrosis,

while other groups presented spherical or spindle tumor cells with abundant chromatin and karyosomes, revealing vigorous proliferation. Notably, necrosis of tumors resected from mice treated with NP/mDs+ α PD-L1 were much more severe than all other groups. Moreover, as indicated by TUNEL assay (Fig. 6f), NP/mDs induced the most extensive DNA fragmentation, further confirming that mDs-cloaking NPs plus α PD-L1 contributed to a significant proliferation arrest *in vivo*.

3.6. Synergistic effect of NP/mDs and α PD-L1 enhanced antitumor immunity

Protein immunoblot analysis was conducted to uncover the apoptotic pathway related to OXA prodrug antitumor therapy. The

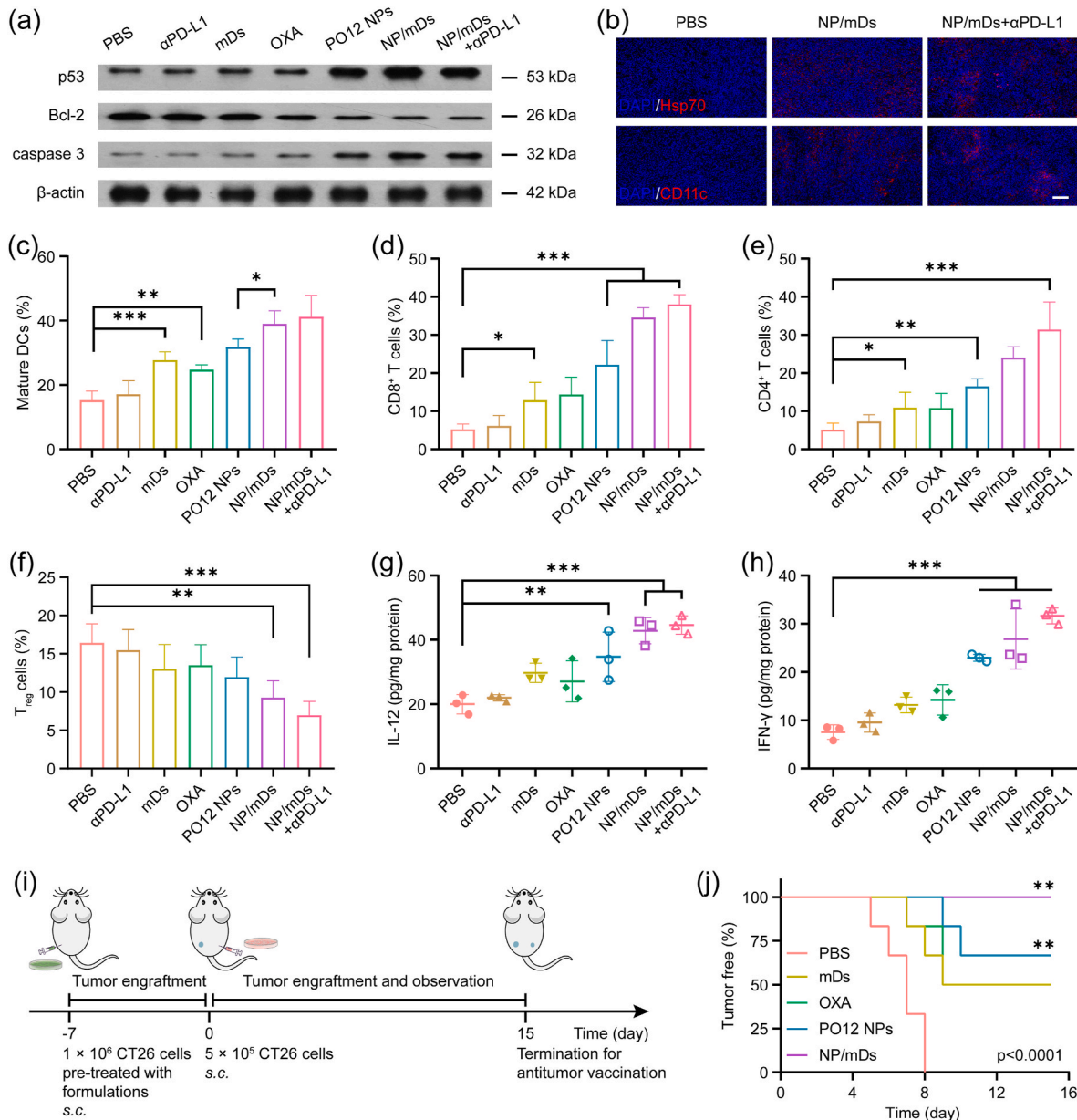


Fig. 7. NP/mDs boosted host immunity for *in vivo* antitumor treatment. (a) Immunoblot analysis of p53, Bcl-2, and caspase 3 of CT26 syngeneic tumors after Q3D \times 5 chemotherapy and/or immunotherapy. β -actin was used as the loading control. (b) CT26 syngeneic tumors after treatment displayed the exposure of ICD makers and the recruitment of APCs. Scale bar = 100 μ m. Percentage of (c) mature DCs, (d) CD8⁺ T cells, (e) CD4⁺ T cells, and (f) Treg cells infiltrated in CT26 syngeneic tumors after mice *i.v.* injected with NP/mDs and each component, and/or *i.p.* injected with α PD-L1 in a Q3D \times 5 schedule, $n = 4$. Release of (g) IL-12 and (h) IFN- γ in CT26 syngeneic tumors, $n = 3$. (i) Schematic representation of dying CT26 cell attenuation and live CT26 cell re-challenge in immunocompetent BALB/c mice for antitumor vaccination evaluation. (j) Percentage of BALB/c mice with tumor-free on the contralateral flank after live CT26 cell re-challenge, $n = 6$. Data points in c-h represent mean \pm SD. Statistical significance was calculated by ANOVA with Tukey's test. n.s., not significant, * $p < 0.05$, ** $p < 0.01$, and *** $p < 0.001$.

cellular suicide mechanism induced by Pt drugs is an orderly process, as it launches the covalent cross-binding between activated Pt and DNA targets, which leads to upregulation of p53 after genetic damage, imbalance of Bcl-2 family proteins, dysfunction of mitochondria, leakage of pro-apoptotic factors, activation of caspase cascade, cleavage of PARP, and finally decomposition of cellular structure. CT26 tumor-bearing BALB/c mice were randomly assigned into separate groups and administered with Q3D × 5 chemotherapy and/or immunotherapy. The comparative expressions of p53, Bcl-2, and caspase 3 in syngeneic tumors were then measured for each group (Fig. 7a). Western blot data revealed the significant upregulation of p53 and caspase 3, and a remarkable downregulation of Bcl-2, especially for the mice receiving combination therapy, supporting the proposed mechanism of mitochondrial control of apoptosis induced by Pt-based chemotherapy.

IF staining of tumor sections was first performed to localize CRT and Hsp70, two critical DAMPs in ICD events (Fig. 7b and S30). Evaluation of fluorescent signals showed that OXA, PO12 NPs, and NP/mDs moderately increased CRT translocation and Hsp70 exposure, but the highest levels of ICD markers were present in the NP/mDs+αPD-L1 group. This observation was consistent with the successful inhibition of CT26 primary tumors and gave a clear hint that the immunogenicity might have evoked leukocytes for immune attack. In view of this matter, CD4⁺ T cells (Helper T cells, CD3e⁺CD4⁺) and CD8⁺ T cells (Cytotoxic T cells, CD3e⁺CD8a⁺) were visualized by IF double staining. As shown in Fig. S30, treatment with PO12 NPs or NP/mDs resulted in high percentages of CD4⁺ and CD8⁺ T cells, while NP/mDs plus αPD-L1 increased the infiltration of T cells much more greatly, demonstrating *in vivo* activation of naive lymphocyte differentiation. In addition, DCs (CD11c⁺) and Macrophages (MΦs, F4/80⁺) inside tumors were also evaluated. The recruitment of the above APCs in response to immunogenic epitopes was maximized in immunochemotherapy groups, particularly the mice receiving NP/mDs and αPD-L1 synergistic therapy. Besides, IF staining of spleens and lymph nodes was also performed to visualize immunocytes (Figs. S31–32). The highest fluorescent signals were found in the NP/mDs+αPD-L1 group, while PO12 NPs and NP/mDs had moderate upregulation of CD4⁺ T cells, CD8⁺ T cells, Memory T cells, and mature DCs.

From the data gained thus far, the antitumor response by combination of immunogenic chemotherapy, TA stimulation, and PD-L1 blockade suggested possible immune modulation. Therefore, immunophenotyping was performed to identify the presence and proportion of leukocyte subpopulations. CT26 tumor-bearing BALB/c mice treated with Q3D × 5 chemotherapy and/or immunotherapy were euthanized and singlet suspensions of tumor tissues after incubating with antibodies were sorted by multiplex flow cytometry (Fig. S33–34). In the TME with secreted DAMPs created by immunogenic chemotherapy and immune molecules provided by mDs, the recruited myelocytes differentiated towards immunopotential phenotypes, e.g., maturation of DCs and depolarization of MΦs. As seen in Fig. 7c–f and S35, the percentage of mature DCs (CD45⁺CD11c⁺CD80⁺CD86⁺) increased from 15.25 ± 2.89% for PBS to 39.05 ± 4.00% for NP/mDs and to 41.18 ± 6.68% for combination therapy. Besides, the percentage of pro-inflammatory M1 MΦs (CD45⁺CD11b⁺F4/80⁺CD86⁺) significantly increased (45.50 ± 7.39% for combination therapy, 40.05 ± 4.64% for NP/mDs, and 14.03 ± 3.38% for PBS), while the proportion of pro-tumorigenic M2 MΦs decreased (8.87 ± 1.64% for combination therapy, 13.23 ± 1.78% for NP/mDs, and 32.75 ± 6.36% for PBS). These results revealed the efficient engulfment of natural TA and sustainable transport of artificial TA to professional APCs. Those tumor-proximal APCs with the created and/or released neoantigen during oncotherapy subsequently presented to cognate T cells to promote tumor-specific innate and adaptive immunity. The integration of NP/mDs and αPD-L1 efficiently increased tumor infiltration by CD8⁺ T cells (CD45⁺CD3e⁺CD4⁺CD8a⁺, 38.00 ± 2.55% for combination therapy, 34.55 ± 2.60% for NP/mDs vs. 5.58 ± 2.85% for PBS) and CD4⁺ T cells (CD45⁺CD3e⁺CD4⁺CD8a⁻, 31.45 ± 7.18% for combination therapy, 24.08 ± 2.81% for NP/mDs vs. 4.30 ± 1.70% for

PBS). Meanwhile, a significant reduction of Regulatory T cells (Treg cells, CD45⁺CD3e⁺CD4⁺CD25⁺Foxp3⁺, 6.97 ± 1.81% for combination therapy, 9.28 ± 2.20% for NP/mDs vs. 16.43 ± 2.48% for PBS) was found, demonstrating that the priming of TA-specific effector lymphocytes and the existence of intratumoral T cell infiltration could further promote the killing effect of NP/mDs.

Several cytokines in tumors were then measured, as they were important molecular messengers to shape the immune microenvironment (Fig. 7g and h). Interleukin-12 (IL-12), mainly produced by phagocytes in response to antigen stimulation, influences the differentiation of naive T cells into effector T cells [40]. Compared with PBS and other control groups, IL-12, secreted by T cells was markedly elevated in CT26 syngeneic tumors treated with NP/mDs (by 5.33-fold over PBS) and NP/mDs+αPD-L1 (by 6.09-fold over PBS). Specifically, CD4⁺ Th1 cells and CTLs are characterized by the ability to produce a first strong wave of IFN-γ, which not only induces a positive feedback loop, but also inhibits tumor growth directly, as antigen-specific immunity develops [41]. Additionally, CTLs purge tumor cells in the primary location and travel throughout the body in search of antigen-positive somatic cells. The utilization of NP/mDs with αPD-L1 led to the highest secretion of IFN-γ (6.74-fold over PBS) in comparison to PBS, suggesting that tumor-infiltrating cytokines contributed to establishing anticancer immunity.

3.7. NP/mDs primed persistent innate and adaptive immune responses

CT26 cells were pre-cultured with NP/mDs and each component *in vitro* for 24 h. The dying cells were then *s.c.* implanted into immunocompetent BALB/c mice as prophylactic vaccines. It was found that most mice injected with either Pt component-exposed or mDs-attached CT26 cells absorbed the dying tumor cells and achieved tumor-free gradually, whereas others developed local solid tumors at the injection flank. One week later, all mice were re-challenged with live CT26 cells on the contralateral flank (Fig. 7i). The absence of tumor growth after live cell injection is interpreted as the sign of a productive antitumor immune response. The mice in the PBS group induced bilateral neoplasia in a natural progression (Fig. 7j), while the mice in the NP/mDs group remained tumor-free, compared to occasional oncogenesis and progression in the OXA and PO12 NPs groups. These results suggested that NP/mDs generated sufficient immunogenic amplification in dying cells to stimulate the adaptive immune response, finally inhibiting secondary tumor engraftment. Interestingly, some mice in the mDs group also initiated the protective antitumor immune response, likely because the mDs-CT26 cell complexes at the primary injection site could recruit myelocytes and license lymphocytes, finally triggering host immunity. The result confirmed that mDs had the ability to induce antigen indirectly cross-dressing and direct presentation.

To further validate the innate and adaptive immune response primed by robust immunogenic chemotherapy and TA-specific immunotherapy, a more aggressive and distant metastasis model was tested with the primary CT26 model. After a Q3D × 5 treatments, CT26 tumor-bearing BALB/c mice were *i.v.* infused with untreated CT26 cells. Once being fed and monitored for ten days post-infusion, the surviving mice were euthanized and lungs were harvested for metastasis analysis (Fig. S36a). Pulmonary metastasis with yellow nodules occurred in all groups. The mice treated with NP/mDs plus αPD-L1, however, displayed the sporadic metastatic lesion with a minimal total number of metastasis nodules (TNMN) (17 ± 14 vs. 187 ± 22 for PBS), indicating superior efficiency of combination therapy in inhibiting distal metastasis, owing to the activation of host immunosurveillance after chemotherapy and immunotherapy (Fig. S37). These results were further confirmed by H&E and Masson's trichrome staining of the collected lung tissues (Fig. S36b). The regimen of NP/mDs plus αPD-L1 presented lungs with significantly decreased tumor cell karyokinesis and increased tumor interstitial fibrosis over other groups, verifying that the activated host immunity was able to inhibit secondary tumor growth and accelerate

focus rehabilitation.

4. Conclusion

In summary, a family of OXA prodrugs with tunable hydrophobicity was developed to formulate with PDEA polymers, with plenty of disulfide bridges, to obtain OXA prodrug-loaded PDEA NPs. Undergoing systemic optimization, PO12 NPs were chosen as the optimal candidate to conduct the biovesicle cloaking process. Isolated mDs, which inherited TA-MHC and costimulatory molecules, maintained the essential immunostimulatory faculties of parent mDCs, which were generated from primary bone marrow and personalized by addition of CT26 tumor lysates in culture. NP/mDs, fused redox-responsive PO12 NPs with biomimetic mDs, were subjected to *in vitro* and *in vivo* evaluation. Following uptake by the tumor, a rapid burst of payloads inside the cytosol occurred in response to redox-mediated polymer disintegration, exhibiting strong potency to inhibit tumor cell proliferation. Data acquired from *in vitro* studies also showed that NP/mDs not only induced immunogenic amplification, but also acted as a native promoter to initiate T cell response through indirect cross-dressing of allogeneic TA to imDCs or direct presentation of TA-MHC, as well as costimulatory molecules, to stimulate lymphocyte activation. Unlike free molecules, NP/mDs, with longer blood circulation, preferentially enriched in tumor sites, therefore alleviating side effects associated with OXA and inhibiting the growth of murine colon carcinoma successfully by mitochondrial apoptosis and immunocyte attack. Additionally, antitumor vaccination and antitumor metastasis revealed that our platform integrated innate and adaptive immune systems to augment host immunity. The biovesicle cloaking strategy simultaneously achieves immune stimulation and selective cytotoxicity, and therefore, proves to be a facile approach to improve the efficacy of current chemotherapy and immunotherapy.

CRedit authorship contribution statement

King Chen: Conceptualization, Methodology, Formal analysis, Investigation, Writing – original draft, Visualization. **Xiang Ling:** Conceptualization, Formal analysis, Investigation, Writing – original draft. **Jiaxuan Xia:** Methodology, Validation, Investigation. **Ying Zhu:** Methodology, Validation, Investigation. **Longlong Zhang:** Methodology, Investigation. **Yuwei He:** Methodology, Investigation. **Anni Wang:** Methodology, Investigation. **Guolong Gu:** Methodology, Investigation. **Bo Yin:** Resources, Writing – review & editing. **Jianxin Wang:** Resources, Writing – review & editing, Supervision, Project administration, Funding acquisition.

Declaration of competing interest

The authors declare that they have no known competing financial interests or personal relationships that could have appeared to influence the work reported in this paper.

Acknowledgements

This work was supported by the National Natural Science Foundation of China (No. 81773911, 81690263 and 81573616), and the Development Project of Shanghai Peak Disciplines-Integrated Medicine (No. 20180101).

Appendix A. Supplementary data

Supplementary data to this article can be found online at <https://doi.org/10.1016/j.bioactmat.2021.12.020>.

References

- [1] W.L. Liu, M.Z. Zou, T. Liu, J.Y. Zeng, X. Li, W.Y. Yu, C.X. Li, J.J. Ye, W. Song, J. Feng, X.Z. Zhang, Cytomembrane nanovaccines show therapeutic effects by mimicking tumor cells and antigen presenting cells, *Nat. Commun.* 11 (1) (2019) 3199–3210, <https://doi.org/10.1038/s41467-019-11157-1>.
- [2] W.L. Liu, M.Z. Zou, T. Liu, J.Y. Zeng, X. Li, W.Y. Yu, C.X. Li, J.J. Ye, W. Song, J. Feng, X.Z. Zhang, Expandable immunotherapeutic nanoplatforms engineered from cytomembranes of hybrid cells derived from cancer and dendritic cells, *Adv. Mater.* 31 (18) (2019) 1–10, <https://doi.org/10.1002/adma.201900499>.
- [3] C.M. Hu, R.H. Fang, K.C. Wang, B.T. Luk, S. Thamphiwatana, D. Dehaini, P. Nguyen, P. Angsantikul, C.H. Wen, A.V. Kroll, C. Carpenter, M. Ramesh, V. Qu, S.H. Patel, J. Zhu, W. Shi, F.M. Hofman, T.C. Chen, W. Gao, K. Zhang, S. Chien, L. Zhang, Nanoparticle biointerfacing by platelet membrane cloaking, *Nature* 526 (7571) (2015) 118–121, <https://doi.org/10.1038/nature15373>.
- [4] A.V. Kroll, Y. Jiang, J. Zhou, M. Holay, R.H. Fang, L. Zhang, Biomimetic nanoparticle vaccines for cancer therapy, *Adv. Biosyst.* 3 (1) (2019) 1–17, <https://doi.org/10.1002/adbi.201800219>.
- [5] Q. Chen, G. Huang, W. Wu, J. Wang, J. Hu, J. Mao, P.K. Chu, H. Bai, G. Tang, A hybrid eukaryotic-prokaryotic nanoplatform with photothermal modality for enhanced antitumor vaccination, *Adv. Mater.* 32 (16) (2020) 1–10, <https://doi.org/10.1002/adma.201908185>.
- [6] X. Han, S. Shen, Q. Fan, G. Chen, E. Archibong, G. Dotti, Z. Liu, Z. Gu, C. Wang, Red blood cell-derived nanoerythrocyte for antigen delivery with enhanced cancer immunotherapy, *Sci. Adv.* 5 (10) (2019) 1–10, <https://doi.org/10.1126/sciadv.aaw6870>.
- [7] J.M. Pitt, F. Andre, S. Amigorena, J.C. Soria, A. Eggermont, G. Kroemer, L. Zitvogel, Dendritic cell-derived exosomes for cancer therapy, *J. Clin. Invest.* 126 (4) (2016) 1224–1232, <https://doi.org/10.1172/JCI81137>.
- [8] C. Thery, M. Boussac, P. Veron, P. Ricciardi-Castagnoli, G. Raposo, J. Garin, S. Amigorena, Proteomic analysis of dendritic cell-derived exosomes: a secreted subcellular compartment distinct from apoptotic vesicles, *J. Immunol.* 166 (12) (2001) 7309–7318, <https://doi.org/10.4049/jimmunol.166.12.7309>.
- [9] L. Zitvogel, A. Regnault, A. Lozier, J. Wolfers, C. Flament, D. Tenza, P. Ricciardi-Castagnoli, G. Raposo, S. Amigorena, Eradication of established murine tumors using a novel cell-free vaccine: dendritic cell-derived exosomes, *Nat. Med.* 4 (5) (1998) 594–600, <https://doi.org/10.1038/nm0598-594>.
- [10] J.M. Pitt, M. Charrier, S. Viaud, F. Andre, B. Besse, N. Chaput, L. Zitvogel, Dendritic cell-derived exosomes as immunotherapies in the fight against cancer, *J. Immunol.* 193 (3) (2014) 1006–1011, <https://doi.org/10.4049/jimmunol.1400703>.
- [11] B. Besse, M. Charrier, V. Lapierre, E. Dansin, O. Lantz, D. Planchard, T. Le Chevalier, A. Livartoski, F. Barlesi, A. Laplanche, S. Ploix, N. Vimond, I. Peguillet, C. Thery, L. Lacroix, I. Zoernig, K. Dhodapkar, M. Dhodapkar, S. Viaud, J.C. Soria, K.S. Reiners, E. Pogue von Strandmann, F. Vely, S. Rusakiewicz, A. Eggermont, J. M. Pitt, L. Zitvogel, N. Chaput, Dendritic cell-derived exosomes as maintenance immunotherapy after first line chemotherapy in nscl, *OncImmunology* 5 (4) (2016) 1–15, <https://doi.org/10.1080/2162402X.2015.1071008>.
- [12] F. Zhou, B. Feng, H. Yu, D. Wang, T. Wang, Y. Ma, S. Wang, Y. Li, Tumor microenvironment-activatable prodrug vesicles for nanoenabled cancer chemioimmunotherapy combining immunogenic cell death induction and cd47 blockade, *Adv. Mater.* 31 (14) (2019) 1–11, <https://doi.org/10.1002/adma.201805888>.
- [13] B. Feng, B. Hou, Z. Xu, M. Saeed, H. Yu, Y. Li, Self-amplified drug delivery with light-inducible nanocargoes to enhance cancer immunotherapy, *Adv. Mater.* 31 (40) (2019) 1–10, <https://doi.org/10.1002/adma.201902960>.
- [14] G. Kroemer, L. Galluzzi, O. Kepp, L. Zitvogel, in: D.R. Littman, W.M. Yokoyama (Eds.), *Immunogenic Cell Death in Cancer Therapy*, 2013, pp. 51–72.
- [15] L. Zitvogel, L. Apetoh, F. Ghiringhelli, G. Kroemer, Immunological aspects of cancer chemotherapy, *Nat. Rev. Immunol.* 8 (1) (2008) 59–73, <https://doi.org/10.1038/nri2216>.
- [16] X. Duan, C. Chan, W. Lin, Nanoparticle-mediated immunogenic cell death enables and potentiates cancer immunotherapy, *Angew Chem. Int. Ed. Engl.* 58 (3) (2019) 670–680, <https://doi.org/10.1002/anie.201804882>.
- [17] X. Ling, X. Chen, I.A. Riddell, W. Tao, J. Wang, G. Hollett, S.J. Lippard, O. C. Farokhzad, J. Shi, J. Wu, Glutathione-scavenging poly(disulfide amide) nanoparticles for the effective delivery of pt(IV) prodrugs and reversal of cisplatin resistance, *Nano Lett.* 18 (7) (2018) 4618–4625, <https://doi.org/10.1021/acs.nanolett.8b01924>.
- [18] S. Wang, G. Yu, Z. Wang, O. Jacobson, L.S. Lin, W. Yang, H. Deng, Z. He, Y. Liu, Z. Y. Chen, X. Chen, Enhanced antitumor efficacy by a cascade of reactive oxygen species generation and drug release, *Angew Chem. Int. Ed. Engl.* 58 (41) (2019) 14758–14763, <https://doi.org/10.1002/anie.201908997>.
- [19] Y.X. Lin, Y. Wang, H.W. An, B. Qi, J. Wang, L. Wang, J. Shi, L. Mei, H. Wang, Peptide-based autophagic gene and cisplatin co-delivery systems enable improved chemotherapy resistance, *Nano Lett.* 19 (5) (2019) 2968–2978, <https://doi.org/10.1021/acs.nanolett.9b00083>.
- [20] T. Wu, J. Liu, M. Liu, S. Liu, S. Zhao, R. Tian, D. Wei, Y. Liu, Y. Zhao, H. Xiao, B. Ding, A nanobody-conjugated DNA nanoplatform for targeted platinum-drug delivery, *Angew Chem. Int. Ed. Engl.* 58 (40) (2019) 14224–14228, <https://doi.org/10.1002/anie.201909345>.
- [21] Y. Lu, A.A. Aimetti, R. Langer, Z. Gu, Bioresponsive materials, *Nat. Rev. Mater.* 2 (1) (2016) 17, <https://doi.org/10.1038/natrevmats.2016.75>.
- [22] J.A. Marin-Acevedo, B. Dholaria, A.E. Soyano, K.L. Knutson, S. Chumsri, Y. Lou, Next generation of immune checkpoint therapy in cancer: new developments and challenges, *J. Hematol. Oncol.* 11 (1) (2018) 39–58, <https://doi.org/10.1186/s13045-018-0582-8>.

- [23] K.M. Hargadon, C.E. Johnson, C.J. Williams, Immune checkpoint blockade therapy for cancer: an overview of fda-approved immune checkpoint inhibitors, *Int. Immunopharm.* 62 (2018) 29–39, <https://doi.org/10.1016/j.intimp.2018.06.001>.
- [24] D.M. Pardoll, The blockade of immune checkpoints in cancer immunotherapy, *Nat. Rev. Cancer* 12 (4) (2012) 252–264, <https://doi.org/10.1038/nrc3239>.
- [25] Y. He, R. Li, H. Li, S. Zhang, W. Dai, Q. Wu, L. Jiang, Z. Zheng, S. Shen, X. Chen, Y. Zhu, J. Wang, Z. Pang, Erythroliposomes: integrated hybrid nanovesicles composed of erythrocyte membranes and artificial lipid membranes for pore-forming toxin clearance, *ACS Nano* 13 (4) (2019) 4148–4159, <https://doi.org/10.1021/acsnano.8b08964>.
- [26] L.M. Wakim, M.J. Bevan, Cross-dressed dendritic cells drive memory cd8+ t-cell activation after viral infection, *Nature* 471 (7340) (2011) 629–632, <https://doi.org/10.1038/nature09863>.
- [27] X. Chen, X. Ling, L. Zhao, F. Xiong, G. Hollett, Y. Kang, A. Barrett, J. Wu, Biomimetic shells endow sub-50 nm nanoparticles with ultrahigh paclitaxel payloads for specific and robust chemotherapy, *ACS Appl. Mater. Interfaces* 10 (40) (2018) 33976–33985, <https://doi.org/10.1021/acsnano.8b11571>.
- [28] X. Chen, L. Zhao, Y. Kang, Z. He, F. Xiong, X. Ling, J. Wu, Significant suppression of non-small-cell lung cancer by hydrophobic poly(ester amide) nanoparticles with high docetaxel loading, *Front. Pharmacol.* 9 (2018) 1–11, <https://doi.org/10.3389/fphar.2018.00118>.
- [29] T.T. Wu, Y. Qi, D. Zhang, Q.L. Song, C.L. Yang, X.M. Hu, Y.L. Bao, Y.D. Zhao, Z. P. Zhang, Bone marrow dendritic cells derived microvesicles for combinational immunochemotherapy against tumor, *Adv. Funct. Mater.* 27 (42) (2017) 1–15, <https://doi.org/10.1002/adfm.201703191>. ARTN 1703191.
- [30] R. Li, Y. He, Y. Zhu, L. Jiang, S. Zhang, J. Qin, Q. Wu, W. Dai, S. Shen, Z. Pang, J. Wang, Route to rheumatoid arthritis by macrophage-derived microvesicle-coated nanoparticles, *Nano Lett.* 19 (1) (2019) 124–134, <https://doi.org/10.1021/acsnanolett.8b03439>.
- [31] D.V. Krysko, A.D. Garg, A. Kaczmarek, O. Krysko, P. Agostinis, P. Vandenabeele, Immunogenic cell death and damp in cancer therapy, *Nat. Rev. Cancer* 12 (12) (2012) 860–875, <https://doi.org/10.1038/nrc3380>.
- [32] A. Serrano-Del Valle, A. Anel, J. Naval, I. Marzo, Immunogenic cell death and immunotherapy of multiple myeloma, *Front. Cell Dev. Biol.* 7 (2019) 1–22, <https://doi.org/10.3389/fcell.2019.00050>.
- [33] O. Leavy, Antigen presentation: cross-dress to impress, *Nat. Rev. Immunol.* 11 (5) (2011) 302–303, <https://doi.org/10.1038/nri2979>.
- [34] C. Thery, L. Duban, E. Segura, P. Veron, O. Lantz, S. Amigorena, Indirect activation of naive cd4+ t cells by dendritic cell-derived exosomes, *Nat. Immunol.* 3 (12) (2002) 1156–1162, <https://doi.org/10.1038/ni854>.
- [35] L. Li, S. Kim, J.M. Herndon, P. Goedegebuure, B.A. Belt, A.T. Satpathy, T. P. Fleming, T.H. Hansen, K.M. Murphy, W.E. Gillanders, Cross-dressed cd8alpha+/cd103+ dendritic cells prime cd8+ t cells following vaccination, *Proc. Natl. Acad. Sci. U. S. A.* 109 (31) (2012) 12716–12721, <https://doi.org/10.1073/pnas.1203468109>.
- [36] P.D. Robbins, A.E. Morelli, Regulation of immune responses by extracellular vesicles, *Nat. Rev. Immunol.* 14 (3) (2014) 195–208, <https://doi.org/10.1038/nri3622>.
- [37] C. Admyre, S.M. Johansson, S. Paulie, S. Gabrielsson, Direct exosome stimulation of peripheral human t cells detected by elispot, *Eur. J. Immunol.* 36 (7) (2006) 1772–1781, <https://doi.org/10.1002/eji.200535615>.
- [38] R. Oun, Y.E. Moussa, N.J. Wheate, The side effects of platinum-based chemotherapy drugs: a review for chemists, *Dalton Trans.* 47 (19) (2018) 6645–6653, <https://doi.org/10.1039/c8dt00838h>.
- [39] R.G. Webster, K.L. Brain, R.H. Wilson, J.L. Grem, A. Vincent, Oxaliplatin induces hyperexcitability at motor and autonomic neuromuscular junctions through effects on voltage-gated sodium channels, *Br. J. Pharmacol.* 146 (7) (2005) 1027–1039, <https://doi.org/10.1038/sj.bjp.0706407>.
- [40] C.S. Hsieh, S.E. Macatonia, C.S. Tripp, S.F. Wolf, A. Ogarra, K.M. Murphy, Development of th1 cd4+ t-cells through il-12 produced by listeria-induced macrophages, *Science* 260 (5107) (1993) 547–549, <https://doi.org/10.1126/science.8097338>.
- [41] R. Thibaut, P. Bost, I. Milo, M. Cazaux, F. Lemaitre, Z. Garcia, I. Amit, B. Breart, C. Cornuot, B. Schwikowski, P. Bousso, Bystander ifn-gamma activity promotes widespread and sustained cytokine signaling altering the tumor microenvironment, *Nat. Can.* 1 (3) (2020) 302–314, <https://doi.org/10.1038/s43018-020-0038-2>.